8-2017

Hyperspectral and Hypertemporal Longwave Infrared Data Characterization

Nirmalan Jeganathan
nj1520@rit.edu

Hyperspectral and Hypertemporal Longwave Infrared Data Characterization

by

Nirmalan Jeganathan, B.E.

THESIS

Presented to the Faculty of the Center for Imaging Science

Rochester Institute of Technology

in Partial Fulfillment

of the Requirements

for the Degree of

Master of Science

in

Imaging Science

Rochester Institute of Technology

August 2017

Signature of the Author _____

Accepted by _____

Coordinator, Degree Program Date

Hyperspectral and Hypertemporal Longwave Infrared Data Characterization

APPROVED BY

SUPERVISING COMMITTEE:

Dr. John Kerekes, Supervisor

Dr. Mike Gartley, Committee Member

Dr. Carl Salvaggio, Committee Member

Acknowledgments

I wish to thank the multitudes of people who helped me to complete this work. First of all, thank-you to the Department of National Defence and the Canadian Armed Forces for providing me this incredible opportunity. Thank-you for my advisor (Dr. Kerekes) and my committee members (Dr. Gartley and Dr. Salvaggio), who were great to work with, for being patient with me and providing me timely feedback to improve my work. Thank-you for my classmates, Tania Kleynhans, Ron Kemker, Eon Rehman and Paul Sponagle for helping with classwork and providing new ideas to improve my thesis. Last, but not least, many thanks to my family for always being there and for their unconditional love and support.

Abstract

Hyperspectral and Hypertemporal Longwave Infrared Data Characterization

Nirmalan Jeganathan, M.S.
Rochester Institute of Technology, College of Science, 2017

Supervisor: Dr. John Kerekes

The Army Research Lab conducted a persistent imaging experiment called the Spectral and Polarimetric Imagery Collection Experiment (SPICE) in 2012 and 2013 which focused on collecting and exploiting long wave infrared hyperspectral and polarimetric imagery. A part of this dataset was made for public release for research and development purposes. This thesis investigated the hyperspectral portion of this released dataset through data characterization and scene characterization of man-made and natural objects. First, the data were contrasted with MODerate resolution atmospheric TRANsmission (MODTRAN) results and found to be comparable. Instrument noise was characterized using an in-scene black panel, and was found to be comparable with the sensor manufacturer's specification. The temporal and spatial variation

of certain objects in the scene were characterized. Temporal target detection was conducted on man-made objects in the scene using three target detection algorithms: spectral angle mapper (SAM), spectral matched filter (SMF) and adaptive coherence/cosine estimator (ACE). SMF produced the best results for detecting the targets when the training and testing data originated from different time periods, with a time index percentage result of 52.9%. Unsupervised and supervised classification were conducted using spectral and temporal target signatures. Temporal target signatures produced better visual classification than spectral target signature for unsupervised classification. Supervised classification yielded better results using the spectral target signatures, with a highest weighted accuracy of 99% for 7-class reference image. Four emissivity retrieval algorithms were applied on this dataset. However, the retrieved emissivities from all four methods did not represent true material emissivity and could not be used for analysis. This spectrally and temporally rich dataset enabled to conduct analysis that was not possible with other data collections. Regarding future work, applying noise-reduction techniques before applying temperature-emissivity retrieval algorithms may produce more realistic emissivity values, which could be used for target detection and material identification.

Table of Contents

List of Tables

List of Figures

Constants

$h = 6.626068 \times 10^{-34}$ Js

$c = 2.99792458 \times 10^{8}$ m/s

$k = 1.3806504 \times 10^{-23}$ J/K

Chapter 1

Introduction and Objectives

And then there was light. And from the beginning of time, light was considered to be pure and singular, until in 1666 Isaac Newton showed that natural light contained colors using two prisms. This knowledge instigated more questions (i.e. What caused the colors? Was light a particle or a wave?) which in turn led to major discoveries made by Newton and other researchers in modern physics and electro-optics [14]. One product of these discoveries and research that we take for granted presently and make use regularly is the camera. Ibn-al-Haytham made a mention of this kind of device in his book, *Book of Optics* in 1021. The first camera was designed by Johann Zahn in 1685, but the first photograph was taken in 1814 by Joseph Nicephore Niepce. Since the earlier cameras were incapable of saving the images, the first practical photography was credited to Louis Daquerre in 1829. Many people then started working on improving this technology, and in 1940, color photography at commercial level started to take effect [9].

The framework for remote sensing, the field of study associated with extracting information about an object without coming into physical contact with it [19], was laid by the discoveries of the interrelations among color,

frequency, and wavelength since these fundamentals principles can be used to characterize the reflection of light against objects. Using these principles and the practical improvements in camera/sensor technology, the integration of remote sensing technology was inevitable once modern aviation became a safe and viable platform. Two strong advocates for remote sensing were the U.S. Departent of Defense (DoD) and the National Aeronautics and Space Administration (NASA) who sponsored the development of many systems. The first class of remote sensors used for aerial photography, reconnaissance, and surveillance were monochrome and panchromatic cameras. In the 1960s, the DoD U-2 reconnaissance planes carried infrared film cameras retroffited with special spectral filters. These cameras were among the first multispectral cameras in existence. In July 1972, NASA launched the Earth Resources Technology Satellite (ERTS), later to be known as Landsat 1, which was the first system capable of producing multispectral (few spectral bands) data in digital format. The advances in computer technology resulted in faster computers that could handle the enormous amount of data collected from new and improved spectrometers, which made the way for hyperspectral (hundreds of spectral bands) remote sensing to flourish in the defense and commercial sectors [14].

Numerous hyperspectral data collects, both ground-based and airborne, conducted by government and commercial sectors produced large datasets, many of them available to the public for research. However, very few collects focused on obtaining data for longitudinal studies (data collected over

a period of time). One such rare longitudinal data collect was the Spectral and Polarimetric Imagery Collection Experiment (SPICE). The SPICE was a collaborative effort between the US Army Research Laboratory (ARL), US Army Armament Research, Develepment and Engineering Center (ARDEC) and the US Air Force Institute of Technology (AFIT) focused on collecting and exploiting long wave infrared (LWIR) hyperspectral and polarimetric imagery. SPICE autonomously collected an expansive dataset of hyperspectral and polarimetric modalities spanning multiple years in a wide range of meteorological conditions. Essentially, hyperspectral and polarimetric sensors continuously imaged a scene approximately every five minutes spanning diurnal cycles and multiple seasons in 2012 and 2013 [35].

This thesis characterizes the SPICE dataset from a top-down perspective. First, the data are validated through computer simulation, the instrument noise characterized, and the temporal and spatial variability of materials examined. Next, the scene is characterized through target detection and classification. Finally, the materials in the scene are identified through emissivity signatures.

Overall, this thesis has two objectives:

Objective 1: Characterize the dataset in detail and conduct comprehensive analysis for further understanding.

Objective 2: Characterize the objects in the scene.

Objective 1 will be accomplished by completing the following tasks:

- Locate and remove erroneous data to improve dataset quality.
- Validate data with MODTRAN.
- Characterize the instrument noise.
- Characterize the temporal variability of materials in scene.
- Characterize the spatial variability of materials in scene.

Objective 2 will be accomplished by completing the following tasks:

- Conduct temporal target detection.
- Conduct hypertemporal classification.
- Retrieve emissivity for material identification.

Chapter 2 describes the SPICE collection, including the location of the collect, the sensor used, the targets in the scene and the data released by ARL. Chapter 3 summarizes previous studies conducted on similar dataset to SPICE and analysis conducted on SPICE dataset. Chapter 4 confirms the data through computer-simulated results, characterizes the instrument noise using an in-scene object, and characterizes the temporal and spatial variation of select materials. Chapter 5 characterizes the scene through temporal target detection and hypertemporal classification. Chapter 6 applies temperature-emissivity algorithms to retrieve material emissivity. Chapter 7 summarizes this thesis and presents future work recommendations.

Chapter 2

Data Set Description

This chapter describes the dataset used in this thesis. It details the purpose and description of the collection, the location of the collect, the sensor used, the targets being imaged, and the calibrated data provided by ARL.

2.1 SPICE Data Collection

Despite a high number of publications on adaptive detection and recognition algorithms produced by geoscience and remote sensing community researchers, a considerable percentage of researchers in this community believed that human innovation and idealized mathematical concepts alone will not solve the pattern recognition problem. Data were indispensible and needed. Especially if different sensing modalities, such as hyperspectral and polarimetric, were to be used for material pattern recognition in remote sensing applications, additional data were essential [35].

The ARL and ARDEC understood this requirement and acted on it. With collaboration from AFIT, ARL and ARDEC collected the SPICE data. SPICE's aim was to collect a comprehensive dataset of hyperspectral and polarimetric modalities spanning multiple years with the intent to capture

sensor performance in a large range of meteorological conditions. The diurnal data were collected with the scene being continuously imaged approximately every five minutes, with about 20 seconds for one image to be captured. A portion of this full dataset was made for public release and disseminated to the open scientific community for algorithmic research and development [35]. The Digital Imaging and Remote Sensing (DIRS) lab from Rochester Institute of Technology (RIT) received a portion of the hyperspectral collect of this released dataset containing several months of data from 2012 and 2013. These data were studied and reported on this thesis.

2.2 Location

The Precision Armaments Laboratory (PAL), located at ARDEC, Picatinny Arsenal, New Jersey (40°55'40.8"N 74°34'52.0"W) specializes in testing sensors under adverse weather conditions. For SPICE, the sensors (hyperspectral and polarimetric) were placed atop the 65-m PAL tower (effective height of 126 m since the tower was positioned atop a 61-m ridge) and the target site area was 549 m from base of the tower (as seen in Figure 2.1). This thesis only covers analysis conducted on data obtained by the hyperspectral sensor. An automated meteorological instrumentation site was located close to the tower, and its measurement instrumentation included wind speed, wind direction, temperature, humidity and barometric pressure [28]. A detailed list of PAL basic meteorological instrumentation types was provided in a previous publication [29].

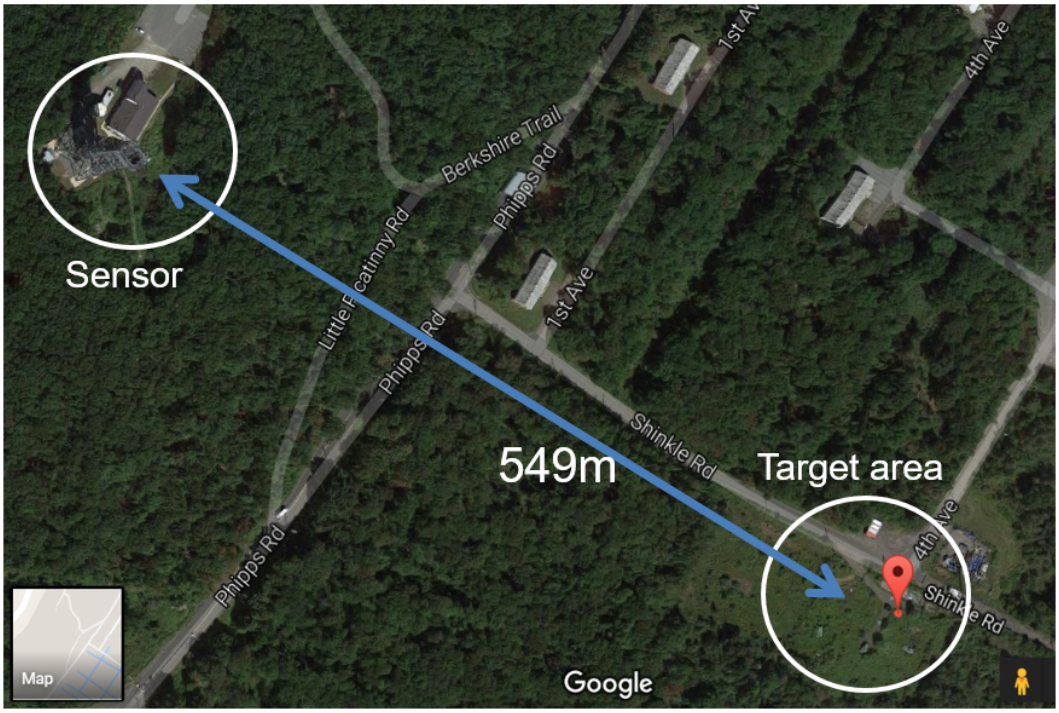

Figure 2.1: The PAL tower, where the sensors were placed, and the target site [3]

2.3 Sensor

The Telops Hyper-Cam Long-Wave (LW) was used for data collection. It was a commercially available lightweight Fourier-transform spectrometer LWIR imager which incorporated a 320 by 256 photovoltaic mercury cadmium telluride (PV MCT) focal plane array (FPA) [35]. Sensor specifications are provided in Table 2.1 [28] and the sensor is shown in Figure 2.2.

Table 2.1: Hyper-Cam LW sensor specification

Region of spectrum (μm)	7.7 to 11.5
Focal length (mm)	86
Cooled FPA	320 by 256
Pixel size (μm)	30
Instantaneous FOV (mrad)	0.35
Black body	Internal (2)
Spectral resolution (cm^{-1})	0.25 to 150
Typical NESR ($nW/cm^2sr{\cdot}cm^{-1}$)	<20

Figure 2.2: Telops LW Hyper-Cam

2.4 Targets

The target site consisted of man-made objects surrounded by natural vegetation. The man-made targets included three surrogate Russian 2S3 howitzers (tanks) oriented in aspect angles of 0°, 90°, and 135° (counterclockwise) with respect to the sensor, a white panel (skyplate/aluminum panel) and a black canvas as shown in Figure 2.3 [35].

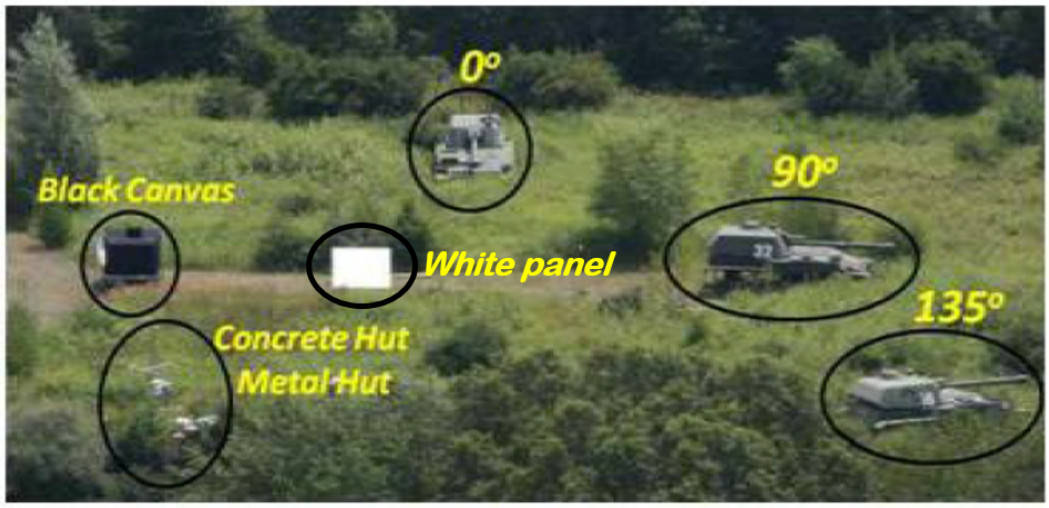

Figure 2.3: Area imaged by Telops Hyper-Cam with a selection of man-made objects labeled, adapted from Rosario et al [35].

2.5 Accessed Data

ARL conducted SPICE spanning two years, 2012 and 2013. The Telops LW Hyper-Cam imaged the target site approximately every five minutes. It took approximately 20 seconds for one image to be captured. The full SPICE dataset contained over 25 000 LWIR hyperspectral data cubes. The meteorological instruments collected data approximately every 2 seconds. The meteorological data were matched with the corresponding Hyper-Cam data in accordance with capture time. All the collected data were processed and delivered in HDF5 file format. Data provided to Rochester Institute of Technology (RIT) for this study included 5855 LWIR HDF5 files, encompassing 18 days from 2012 and 8 days from 2013 (described in Table 2.2).

2.5.1 Processed Data

ARL received the SPICE raw data and its corresponding blackbody raw data in HDF5 file format. These files were used to generate calibrated files via IDL software written by Dr. Christoph Borel-Donohue [13]. A Quick Temperature-Emissivity Separation (QTES) algorithm was applied to retrieve the emissivity [12] [13]. All calibrated data were written in HDF5 file format. The data in each HDF5 file provided by ARL had, among other data, three hyperspectral cubes: calibrated spectral radiance, brightness temperature and relative emissivity. Each 2012 data cube had 256 $\times$ 320 pixels $\times$ 165 bands. The 2013 data had its spatial window size altered and its dimensions were 224 $\times$ 300 pixels $\times$ 165 bands. The 165 bands corresponded to wavelengths between 7.4081 μm and 12.4493 μm. Due to sensor limitations, only 105 bands were used in this analysis by omitting the first 30 and the last 30 bands. The 105 bands corresponded to wavelengths between 8.00075 μm and 11.0712 μm.

2.5.1.1 Radiance

The metadata and few publications ([35] [31]) indicated that the provided spectral radiance was in W/m^{2}sr$\cdot$cm^{-1}. However, it was discovered that the spectral radiance was in fact in W/m^{2}sr$\cdot\mu$m. A sample spectral radiance image is shown in the top left portion of Figure 2.6.

The first step was to recreate some published graphs. Figure 2.4 is an extract from [35], produced from data obtained on 5 July 2012 at 13:11hrs. Figure 2.5 is a pseudo-recreated image of Figure 2.4 (since the exact time-

frame data were not available, the recreation used data from 5 August 2012 at 13:09hrs, approximately one month apart). It could be seen that both figures show the same trend in material spectral radiances.

The spectral radiance unit was confirmed by calculating the brightness temperature from the spectral radiance data and comparing it with the provided brightness temperature data.

2.5.1.2 Brightness Temperature

The brightness temperature was calculated using the inverse Planck equation (Eq. 2.1)

$$T_{\lambda,L_\lambda} = \frac{hc}{\lambda k \ln(\frac{2hc^2}{\lambda^5 L_\lambda} + 1)} \tag{2.1}$$

where T_{λ,L_λ} is the brightness temperature in K, h is the Planck constant (6.626068×10^{-34} Js), c is the speed of light (2.99792458×10^8 m/s), k is the Boltzmann constant ($1.3806504 \times 10^{-23}$ J/K), λ is the wavelength in m and L_λ is the spectral radiance in W/(m^2srm). A sample brightness temperature image is shown in the top right portion of Figure 2.6.

The brightness temperature obtained using Eq. 2.1 and the radiance cube yielded very close values to the brightness temperature cube provided in the HDF5 file. The reason for the minute discrepancy could be attributed to the number of significant digits used in the constants.

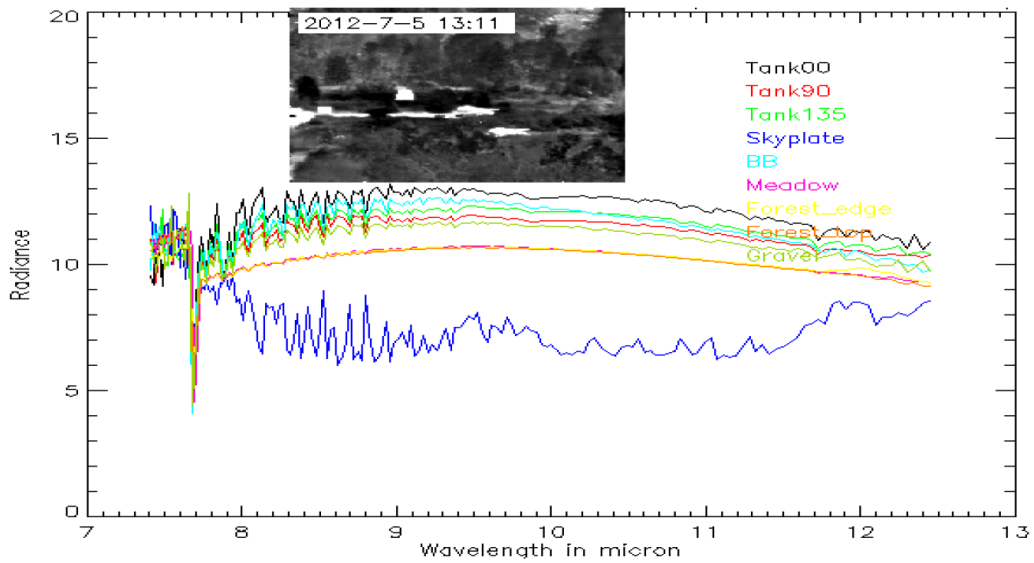

Figure 2.4: Bottom Fig. 11 from Ref [35] showcasing average spectral radiance for select material subsets.

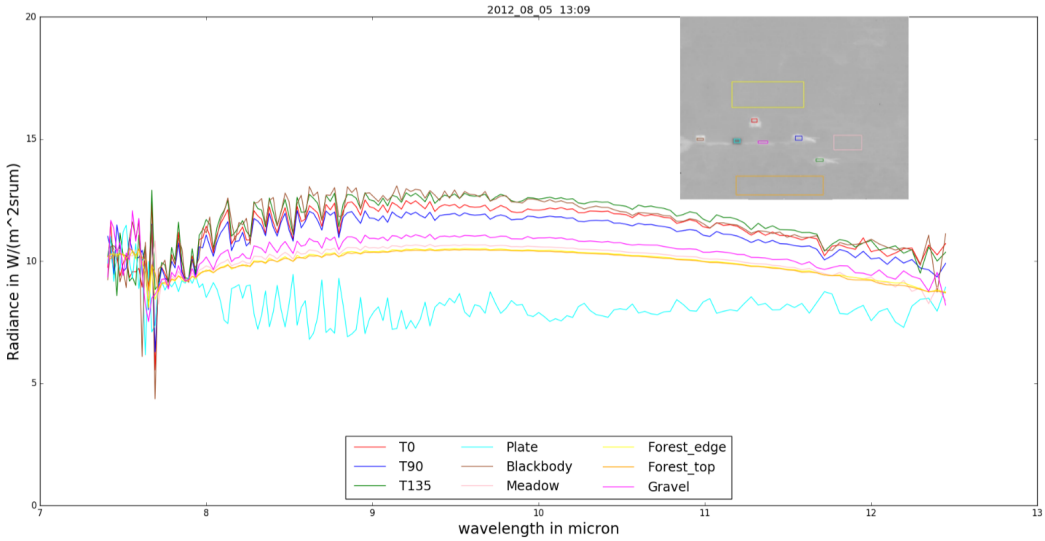

Figure 2.5: Pseudo-recreation of Figure 2.4

2.5.1.3 Relative Emissivity

Emissivity is defined as the ratio of the energy radiated from a material's surface to that radiated from a blackbody at the same temperature and wavelength and under the same viewing conditions. It is a dimensionless number between 0, for a perfect reflector, and 1, for a perfect emitter [1]. One of the provided data cubes was the relative emissivity; it was calculated using the skyplate from the scene and considering it to be a perfect reflector. Relative emissivity was the result of the Quick Temperature-Emissivity Separation (QTES) algorithm, which is described in detail in Section 6.1.3. A sample relative emissivity image is shown in the bottom left portion of Figure 2.6. For better visualization, the sample relative emissivity data were normalized following histogram equalization (shown in bottom right portion of Figure 2.6). The provided relative emissivity cubes consistently had values greater than 1, which were not physically possible for material emissivity. To ensure that errors were not made during the calculation of relative emissivity by ARL and to validate the QTES algorithm, the QTES alogrithm was implemented step-by-step using the provided data as explained in Section 6.1.3.

2.5.2 Material Mask

There were several materials in the scene, both man-made (tanks, black canvas, skyplate) and natural (trees, grass, gravel). In order to identify each pixel with a specific material, materials masks were created using the Region of Interest (ROI) tool from ENVI. However, despite using the same sensor and

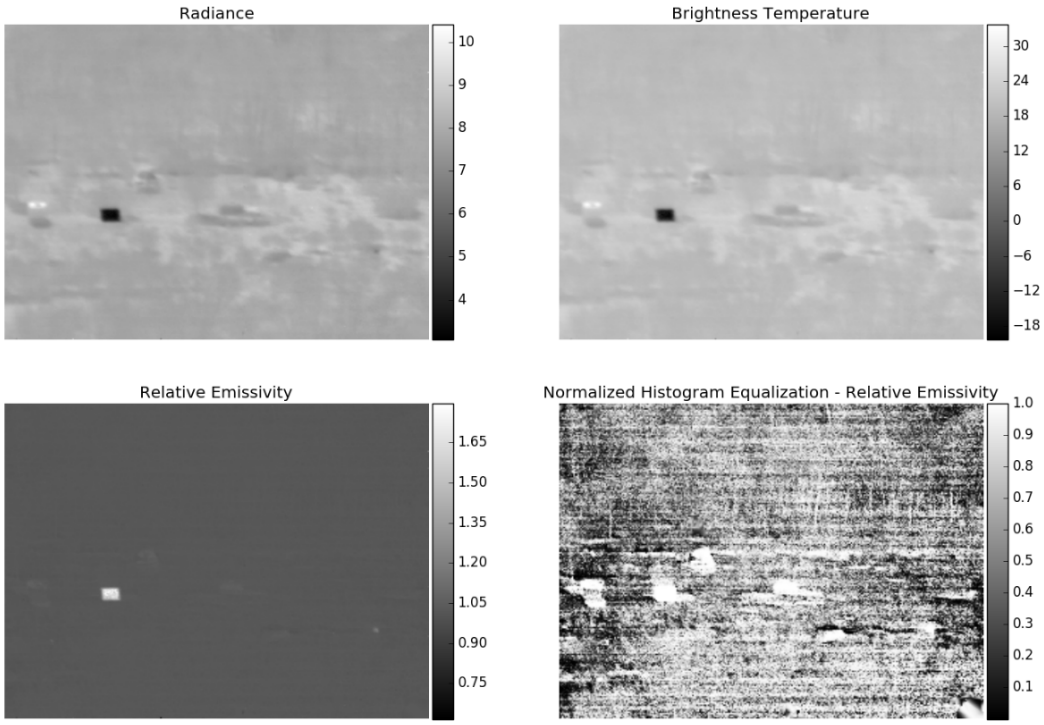

Figure 2.6: Top left: Spectral radiance image (W/m^{2}sr·μm). Top right: Brightness temperature image (°C). Bottom left: Relative emissivity image. Bottom right: Histogram equalized relative emissivity image for better visualization of the scene.

imaging the same scene, the 2012 and 2013 data had different spatial window sizes. Figures 2.7 and 2.8 display the masks created to categorize the different materials in the scene for each year's data.

2.5.3 Data Screening

While studying the dataset, it was observed that some data had inconsistent behavior. An example of inconsistent result was a plot of diurnal

Figure 2.7: Material masks (Tank0 [red], Tank90 [purple], Tank135 [blue], black panel [black], aluminum panel [white], gravel [gray], near-trees [light green], rear-trees [dark green], bush [yellow] and grass [brown]) for 2012 data.

Figure 2.8: Material masks (Tank0 [red], Tank90 [brown], Tank135 [yellow], black panel [black], aluminum panel [white], gravel [purple], near-trees [dark green], rear-trees [light green], bush [dark purple], grass [gray] and miscellaneous background [aqua]) for 2013 data.

brightness temperature variation of the data. As observed in Figure 2.9, there were "periodic" data spikes occurring throughout the plot. The following steps were carried out to explore this observation further:

1. Plot a brightness temperature pixel of one tank for a selected band for all cubes in one day (see Figure 2.9).

2. Determine the "inconsistent" cubes using the plot (i.e. cubes producing "spikes" were inconsistent).

3. Individually verify each inconsistent cube to confirm if the whole cube is inconsistent (the inconsistencies were determined by comparing the

brightness temperature of vegetation pixels of said cube with its neighboring cubes). It was discovered that all image pixels generated the spikes for certain cubes and this behavior was not limited to the selected tank pixel.

4. Repeat for all available data days.

5. Tabulate inconsistent cubes.

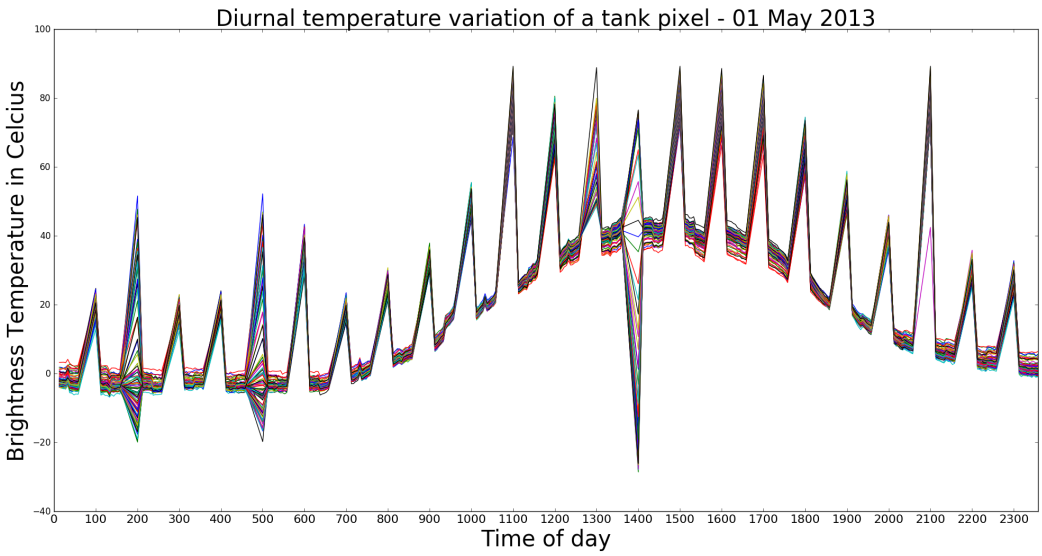

Figure 2.9: 01 May 2013 diurnal brightness temperature of a tank pixel. Y-axis correspond to brightness temperature (°C), x-axis correspond to the 24-hrs duration of a day and the multiple plots correspond to 105 spectral bands. It was noted that all bands spike for certain time index cubes.

It was observed by ARL that the data cubes collected immediately after the automatic hourly blackbody measurements had a low probability of being reliable data [30]. These inconsistent data cubes corresponded to

such measurement times. A total of 339 cubes of the dataset studied were identified as inconsistent (as per Table A.1 in Appendix A), and these cubes were removed from further analysis for this thesis.

Table 2.2: Available SPICE dataset

Date	Number of hdf5 files
2012_07_27	146
2012_07_30	154
2012_07_31	208
2012_08_01	264
2012_08_02	264
2012_08_03	264
2012_08_04	264
2012_08_05	264
2012_08_06	264
2012_08_07	193
2012_08_10	165
2012_08_11	264
2012_08_12	264
2012_08_13	264
2012_08_14	264
2012_09_04	96
2012_09_05	262
2012_09_06	264
2013_05_01	263
2013_05_02	263
2013_05_03	263
2013_05_04	263
2013_05_05	263
2013_05_06	146
2013_05_07	172
2013_05_08	94

Chapter 3

Related Literature

SPICE was a hyperspectral (HSI) longwave infrared (LWIR) dataset collected with a temporal aspect (over a long period of time). The three major aspects of SPICE were HSI, LWIR and temporal data. This section reviews some past publications that have used HSI, LWIR or temporal data in their studies. It also analyzes previous studies that have used the SPICE data, as well as studies that handled hypertemporal data.

3.1 Previous Studies on Data Similar to SPICE dataset

There is a large amount of HSI datasets available for research. The variety within them is immense, including a difference of platform used to image the target (ground-based vs airborne vs satellite), the distance between the sensor and objects (meters vs kilometers), the spectral regions of the sensor used, and the various materials being imaged (man-made objects vs natural vegetation vs living beings).

Some popular airborne/satellite based HSI with ground-truth included are the Indian Pines, Salinas, and Pavia Centre and University datasets [6]. An interesting ground-based dataset released by T. Skauli and J. Farrell was

the "faces" dataset (in addition to the test scene and outdoor scenes) which imaged about 70 subjects using VNIR and SWIR sensors [38]. There are many other sources to obtain free HSI datasets; for example SpecTIR provides many sample datasets on their website [7].

3.1.1 Hyperspectral Images

R. Marwha et al [27] used data collected using the same sensor manufacturer as the SPICE dataset (Telops' Hyper-Cam) for classification. However, this image's spatial resolution (1 m) and spectral resolution (6 $cm^{-}1$) were different from SPICE's setting, and they used an airborne platform to collect data of the Thetford Mines, located in Quebec, Canada on May 2013. Only one HSI cube was used for this study, unlike SPICE, temporal data were not collected. The LWIR data collected had 84 bands (7.8 to 11.5 μm) and were noisy. They applied Minimum Noise Fraction (MNF) on the thermal data and tested eight pixel-based classifiers. They obtained an overall high accuracy of 90.99% using the Spectral Angle Mapper (SAM) algorithm.

Another example of using HSI was done by Zhang and Sriharan [40]. They used data acquired by Airborne Visible-Infrared Imaging Spectrometer (AVIRIS) on July 1999 of the Stennis Space Center. Their data covered 0.3704 to 2.5101 μm range in 224 spectral bands. The AVIRIS image spectra were compared to the spectral library provided by three different agencies and labs (1. The United States Geological Survery Vegetation Spectral Library, 2. Jasper Ridge Spectral Library for Green Vegetation, Dry Vegetation, and

Rocks, and 3. The John Hopkins University Spectral Library for Man Made Materials, and Vegetation). Visual analysis, as well as spectral analysis using ENVI were carried out. They concluded that it was extremely difficult to identify vegetation species by spectral analysis itself, and that the vegetation spectra changes due to season, climate, environment and growding condition. They also identified a need for more timely data, and ground sampling and truthing to verify their identified results.

3.1.2 Longwave Infrared

Another major aspect of the SPICE dataset was thermal LWIR. HSI in this spectral regime (8-12 μm) provide a useful tool in studying gaseous materials. Typically, molecular gases exihibit a unique spectral absorption features in LWIR that could potentially be used for both detection and identification of these gases, assuming a sensor with appropriate spectral response acquired the data with a low background emissivity [25].

As such, M. Chilton et al [15] conducted chemical detection using LWIR HSI. However, due to extreme difficulty and cost in attaining the level of control of all variables in the natural environment, computer-simulated HSI was used to conduct their analysis. The InfraRed Systems Analysis General Environments code (IR-SAGE) developed at Pacific Northwest National Laboratory (PNNL) was used to simulate LWIR hyperspectra of simplified gaseous plumes over organized background pixels. Their objective was to explore how well their metrics predicted when a chemical would be detected when com-

paring one background type to another. Their two predictor metrics correctly ranked the backgrounds for about 94% of the chemicals tested.

3.1.3 Temporal Data

Although HSI and LWIR were major aspects of SPICE dataset, the specialty of SPICE rests in its temporal collection. Yet, even temporal data are not unique, nor a novel concept. Three studies with varying temporal collections are described in this section.

T. Marrinan et al [24] used a Fabry-Perot Interferometer Sensor Data Set that included temporal information, in the sense that it was LWIR data of 4-dimensional array (256 rows $\times$ 256 columns $\times$ 20 bands $\times$ 561 frames). The spectrometer used to collect this data operated in the 8-11 μm range. For this study, they burst Triethyl Phosphate (TEP) gas near frame 111 of the movie and a flag-based algorithm was carried out to detect the gas signature. Their flag-based algorithm performed better than Adaptive Cosine Estimator (ACE) and Matched Filter (MF) algorithms in detecting the released gas. Although the temporal duration of this dataset was not specified, it could be argued that it was minuscule (only 561 movie frames, therefore in terms of minutes at most) compared to the SPICE data which contained temporal data spanning multiple years.

Another example of utilizing temporal data for their study was carried out by A. Lausch et al [23] to monitor chlorophyll, leaf area index, and water content of barley during a growing season. The AISA-EAGLE (400-700 nm,

252 spectral bands) collected spectral data twice a week for over a three-month period from 27 April 2009 to 20 July 2009 under controlled environmental conditions. The time interval between data acquisitions for this study was days and the total duration of the collection was months, while SPICE's acquisition interval was in minutes that lasted multiple years. Another prominent difference between the two collections was that AISA-EAGLE was VNIR while the Telops Hyper-Cam was LWIR.

A dataset somewhat similar to the SPICE data in terms of longitudinal study was collected by J.E. Johnson et al [21] to detect CO_2 gas leak. They used FLIR Systems Inc Photon 320 camera (320×256 LWIR thermal imaging camera) to acquire images every 10 minutes throughout each day for the 2009 CO_2 gas release period, every 5 minutes in 2010, and every 1 minute in 2011 at the Zero Emissions Research and Technology (ZERT) field in Bozeman, Montana. The gas release period in the ZERT field lasted approximately only one month each year. Although this was not HSI, the acquisition time interval from 2010 was comparable to SPICE's, and the acquisition time interval from 2011 was finer than SPICE's acquisition time interval of five minutes.

3.2 Previous Studies on SPICE dataset

Despite having many publications on LWIR, HSI and temporal data, not many dataset were available that incorporated all three aspects like the SPICE dataset. The SPICE dataset has been studied and analyzed by ARL for the last few years. The hyperspectral sensor used was a lightweight and

compact imaging radiometric spectrometer manufactured by Telops. According to the manufacturer, the sensor was employed during SPICE in a setting of continuous and autonomous data collection for the very first time in this product's history - all sensor parameters were set to fixed values regardless of time of day, weather condition, etc. Therefore, one of the initial assessments done by ARL was to characterize the quality of the data obtained by the sensor. The LWIR Hyper-Cam used in SPICE underwent a 30-days period basic assessment at AFIT prior to the data collection at ARDEC [31, 34]. The results were compared with another Telops LWIR Hyper-Cam owned by AFIT. The AFIT's model, despite being similar to the one used in SPICE, had higher spectral resolution. Both sensors were employed in the same indoor lab setting and limited outdoor experimentations. The AFIT owned sensor had also collected data on the same target area in 2011, but for limited daytime period only. Enabled by the small amount of data collected in 2011, AFIT collection employed a human operator monitoring the collection and making appropriate sensor parameters adjustments as per changing conditions in the scene to maximize data quality (e.g., integration time, optical focus). The average spectrum per material type for the two classes, manmade (e.g., tanks) and natural (e.g., vegetation, gravel), were plotted for July 2011 and July 2012, and the spectral profiles were found to be comparable between both data cubes.

Further reassurance regarding the SPICE dataset quality was obtained through comparison with MODerate resolution atmospheric TRANsmission

(MODTRAN) model [31, 34], a computer program that models atmospheric propagation of electromagnetic radiation in the spectral range between 0.2 and 100 micron. The surface-reflected downwelling sky radiance, retrieved from the skyplate located at the SPICE scene, corresponded to downwelling sky models featured in MODTRAN. The quality of the Hyper-Cam was also compared with far more expensive sensors, notably the Air Force sponsored Spatially Enhanced Broadband Array Spectrograph System (SEBASS) LWIR hyperspectral instrument, and the Hyper-Cam data was found to be far more noisier. Despite being noisier than other datasets collected with expensive sensors, the SPICE dataset formed a unique dataset, rich in spectral content and temporal variation.

A major algorithm test was carried using the anomaly detection algorithms, notably the Range-Invariant Anomaly Detection (RIAD) and Reed-Xiaoli anomaly detection (RXD) algorithms [11, 13]. The published result used the data obtained in 2011 by AFIT's Hyper-Cam to test these algorithms, however, since the data were comparable with ARL's Hyper-Cam as discussed previously, they are included for completeness. In this case, manmade objects (tanks and panels) were considered to be anomalies. When RIAD was applied on the radiance and the brightness temperature data, the anomalies were detected quite easily. However when it was applied to the relative emissivity data, only the skyplate was detected as an anomaly since its emissivity was low, but the tanks' emissivities were too similar to the background. Better results were expected from both the global and local RXD, but they failed ex-

pectations. Both the global and local RXD detected the skyplate on radiance, brightness temperature and relative emissivity data. However, the tanks were not found by either global or local RXD using any of the data types. The RXD algorithm was run again by omitting the skyplate pixels, but that did not improve the performance.

Target detection of the tank paint was performed using two methods: single-class Support Vector Machine (SVM) and a longitudinal data model based classifier [32]. The full diurnal cycle target spectrum of the tank paint (Tank0, Tank90 and Tank135) was used to train the two methods. The single-class SVM function returned +1 for the training data points (target) and -1 elsewhere (background). The longitudinal study was defined as objects being measured repeatedly through time, and as a result, data were dependent. Thus, the longitudinal model took into account the correlation of the samples across time. It took the spectral and temporal information of one diurnal cycle of all three tanks during training. The test results were quantified using three consecutive days data (426 data cubes) - daytime and nighttime - in the x-axis and the probability of detection on the y-axis. The first diurnal cycle corresponded to the training data, while the two remaining diurnal cylces corresponded to the test data (data not seen by the methods before the test). The single-class SVM had higher detection rate during the daytime period compared to nighttime period. The longitudinal model detected the three tanks significantly higher than the single-class SVM regardless of the time period. It was noted that the longitudinal model employed in this study used

the temporal data collected over three diurnal cycles, but did not form a temporal signature for target detection.

Rauss and Rosario studied the generalization and scalability behavior of a deep belief network (DBN) applied to the SPICE dataset [26]. They used conditional receiver operating characteristic (ROC) curve to quantify deep learning performance. Their study, however, raised more questions than answers for employing classifiers based on artificial neural networks to train and test on spectra representing multiple material classes under changing diurnal conditions.

The quality of SPICE dataset was verified with MODTRAN results and compared with similar sensor results. Two major algorithms carried out with this dataset were anomaly detection and target detection. The published results frequently used the calibrated radiance to conduct the analysis, but not much work had been carried out using material emissivity. One way to augment the existing knowledge on the SPICE dataset is to use emissivity for target identification. In addition, performing target detection using conventional algorithms will supplement the results observed by D. Rosario et al [32].

3.3 Hypertemporal Data Studies

A special aspect of this dataset was its temporal information; persistent imaging of a scene over time. Hyperspectral can be defined as over sampling of spectral data (hundreds of spectral bands). Likewise, hypertemporal can be

defined as over sampling of temporal data (hundreds of time indexes). However, hypertemporal imaging is not a novel topic. For starters, the time series images could be constructed using the daily imagery acquisitions provided by sensors such as Moderate-Resolution Imaging Specrometer (MODIS), and the National Oceanic and Atmospheric Administration (NOAA) Advanced Very High Resolution Radiometer (AVHRR). Coppin et al [16] used such data to conduct bi-temporal (between two pairs of images) and temporal trajectories (between time profiles) change detection of an ecosystem. They concluded that the major drawbacks were the coarse spatial resolution of the imagery and the limitations on the available time series.

Bie et al [17] used hypertemporal images for crop mapping and classification. They used 10-day composite 1-km resolution SPOT-Vegetation NDVI images of six global locations to carry out this study. Their results included maps showing the spatial-temporal characteristics of the findings.

ATK, an American aerospace, defense and sporting goods company (now Orbital ATK) developed a high-speed Michelson FTIR ground-based sensor capable of collecting chemical spectra at 1000 interferograms per second at 4 cm^{-1} spectral resolution [18]. In 2010, they initiated an effort to space qualify this product and seek a small satellite mission to carry this payload.

The government sector also showed interest in space-based hypertemporal imaging. In April 2014, the US's Air Force Laboratory's Space Experiments and Programs Branch announced a $33.7 million, five-year contract to Raytheon for a payload testing the concepts of persistent surveillance of

the Earth from space. This payload, the Hypertemporal Imaging Space Experiment, will fly on the ESPA Augmented Geostationary Laboratory Experiment's (EAGLE) platform bus [4].

The SPICE data was used for hypertemporal target detection methods by Rosario and Romano [33]. They used four methods to train and detect the tanks' paint, and they concluded that detectors based on the estimation of fixed parameters do not perform well with hypertemporal data.

3.4 Motivation for this Thesis

The SPICE dataset was made for public release and disseminated to a large number of research community. Despite this action, the most notable publications using this dataset remained authored by ARL researchers. It was understood that this dataset can be analyzed with a fresh perspective, adding to the results published by ARL. Foremost, the results published by ARL can be validated by an outside party not related to the data collection. Almost all ARL publications exclusively used the spectral radiance data, the emissivity data could be used for further analysis. The hypertemporal target detection studied by [32] and [33] could be further explored. Thus, these open venues of research motivated the work described in this thesis.

Chapter 4

Data Characterization

This chapter characterizes the SPICE data obtained from ARL. To gain initial confidence in the data, they were first compared to a computer simulated program, MODTRAN. Once the MODTRAN results confirmed the data, further analysis was done including characterizing the instrument noise. The temporal and spatial characteristics of the data were then explored.

4.1 Impacts of Precipitation

The SPICE data were collected during various meteorological conditions. This subsection explored the differences observed in one diurnal cycle with changes in precipitation as categorized by: no precipitation, light hail, light rain, moderate rain and heavy rain.

Figure 6 from reference [34] (Figure 4.1) was recreated for the different meteorological instances to compare the effects of precipitation. The effects of precipitation on the collected data were assessed by comparing the spectral signatures of select materials during varying meteorological conditions. Figure 4.2 shows the subset of each material used for this analysis.

The diurnal data from 1 August 2012 were used for this analysis. This

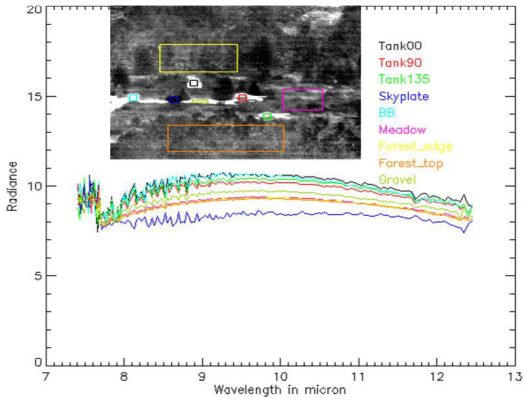

Figure 4.1: Figure 6 from reference [34]

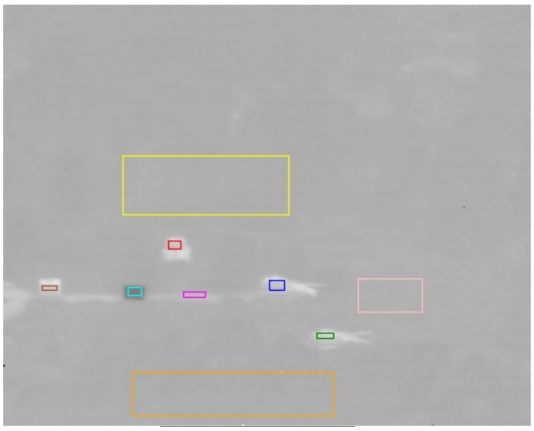

Figure 4.2: Subset of materials used for analysis

date was chosen primarily because it contained the five different precipitation classes described for collection by ARL. All 165 bands from the data cubes provided by ARL were used in this analysis. For visualizing the changes, the band corresponding to 10.1 μm was displayed.

Figure 4.1 displays the daytime radiance effect for the different materials. Figure 4.3, which used the noon timeframe data, shared similar material trends with Figure 4.1. Since it was a sunny with no precipitation at noon timeframe, conditions were ideal for data collection. As observed in Figure 4.4, all three tanks, the two panels and the gravel were visible and distinguishable from the surrounding vegetation. Even within the vegetation, separation can be seen between trees, bushes and grass.

Figures 4.5 and 4.6 show the results for data captured with light hail. There were drastic differences between Figures 4.3 and 4.5. One reason for this

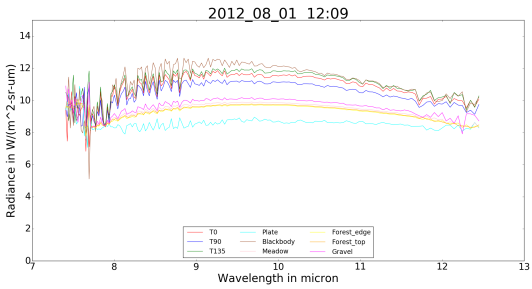

Figure 4.3: Average spectral radiance for nine materials in the scene observed on 1 Aug 2012 at 12:09, with no precipitation.

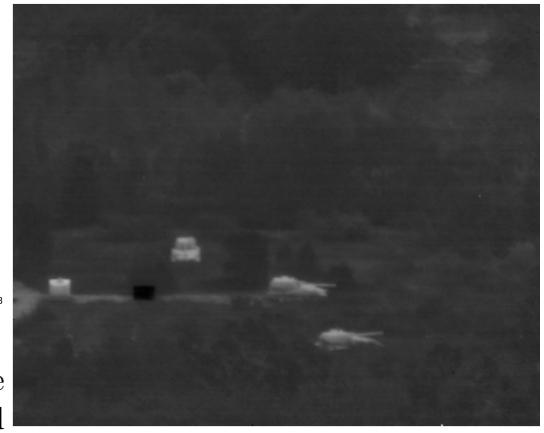

Figure 4.4: Band 10.1 μm from 1 Aug 2012, 12:09, calibrated radiance cube.

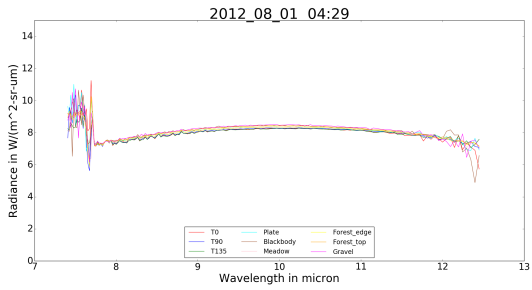

Figure 4.5: Average spectral radiance for nine materials in the scene observed on 1 Aug 2012 at 04:29, with light hail.

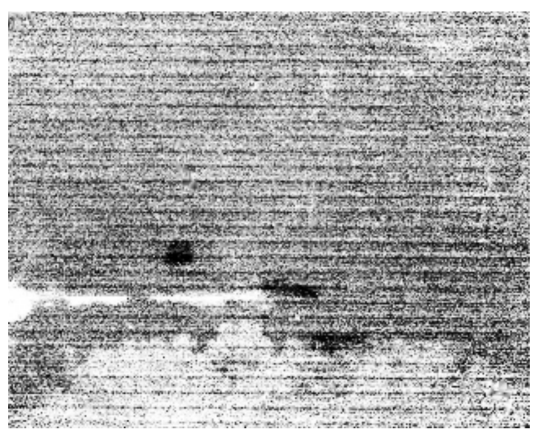

Figure 4.6: Band 10.1 μm from 1 Aug 2012, 04:29, calibrated radiance cube (histogram equalized to accentuate contrast).

difference is that the data were captured at different times of day, 04:29 and 12:09. Figure 4.3 displays different spectral signatures for various materials, while Figure 4.5's spectral signatures for the same materials are similar to each other. In addition, there was light hail during the capture of data at 04:29, which may also be a factor for these differences. Visually, the materials in the scene were indistinguishable from one another, therefore, the image was histogram equalized in order to accentuate contrast to identify some objects in the scene as observed in Figure 4.6.

Light rain had less effect on the sensor collection than light hail. This could be due to the hard pellets of frozen rain compared to the liquid rain affecting the atmospheric transmission. Figure 4.7 showed spectrally different trends between the materials, albeit not as much as the noon no-precipitation timeframe. Figure 4.8 separated the man-made objects and the gravel from the vegetation, however, differences within the vegetation were not observed.

The moderate and heavy rain data were collected during the early part of the day (04:39 and 05:58). During the early part of the day, the sun would not have had enough time to heat some of the materials (i.e. tanks and rocks) to generate thermal differences between them and vegetation (materials that would not heat as much). Therefore, it was expected that much spectral differences between the materials not to be observed, as seen in Figures 4.9 and 4.11. The effects of moderate and heavy rain could also be observed in Figures 4.10 and 4.12, where none of the materials in the scene are distinguishable.

This subsection showed us two findings. First, during light hail, mod-

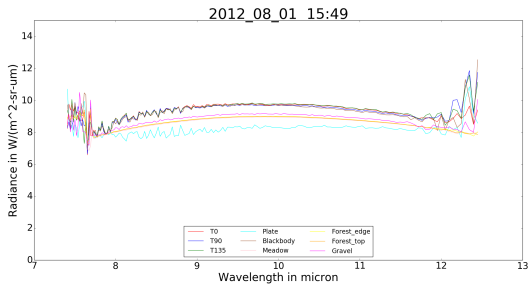

Figure 4.7: Average spectral radiance for nine materials in the scene observed on 1 Aug 2012 at 15:49, with light rain.

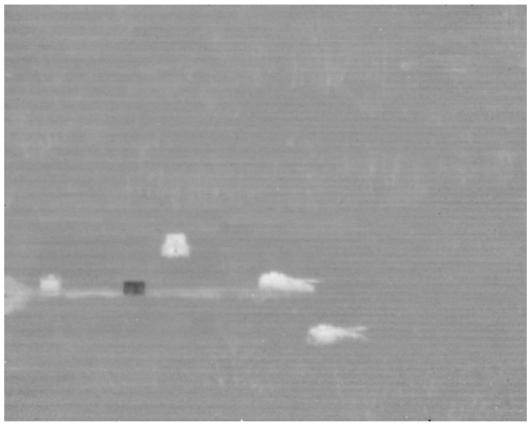

Figure 4.8: Band 10.1 μm from 1 Aug 2012, 15:49, calibrated radiance cube.

erate and heavy rain, the spectral radiances between different materials are too similar to one another as seen in Figures 4.5, 4.9 and 4.11. This was also visually observed in Figures 4.6, 4.10 and 4.12 where the scene was essentially uniform with almost non-existing features before histogram equalization. Yet, even after histogram equalization, real separation between materials were not observed within the scene, which were noisy images. At the same time, the indistinguishable features cannot totally be attributed to hail and rain. Since these data were collected during a time prior to solar heating of the scene, they were not comparable with the no-precipitation (noon timeframe) data. The best method to compare the effects of precipitation would be to have moderate and heavy rain data collected during daytime and compare with similar timeframe no-precipitation data. However, within the data provided by ARL, there was no moderate or heavy rain during daytime.

Another finding from this subsection were observed in Figures portray-

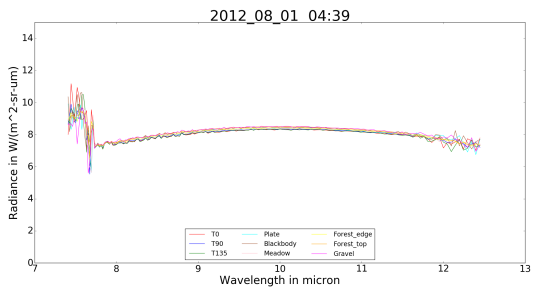

Figure 4.9: Average spectral radiance for nine materials in the scene observed on 1 Aug 2012 at 04:39, with moderate rain.

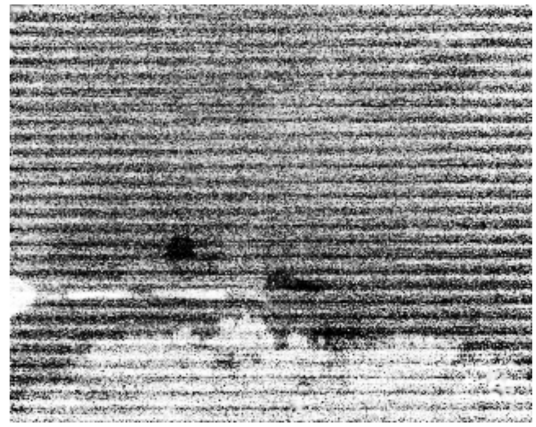

Figure 4.10: Band 10.1 μm from 1 Aug 2012, 04:39, calibrated radiance cube (histogram equalized to accentuate contrast).

ing the spectral radiances of the scene materials. ARL recommended to not use the first and last 30 bands of this collection due to the high noise in these bands. This recommendation was validated since it was observed that when all 165 bands were plotted, the beginning and end portions of the spetrum did not follow the trend observed in the 8-11 μm range, but behaved more like noise.

4.2 MODTRAN Confirmation

One action carried out was to validate the obtained data, to ensure they were realistic and dependable for further analysis. This validation was done through MODTRAN simulation, a computer code that is used worldwide by research scientists for the prediction and analysis of optical measure-

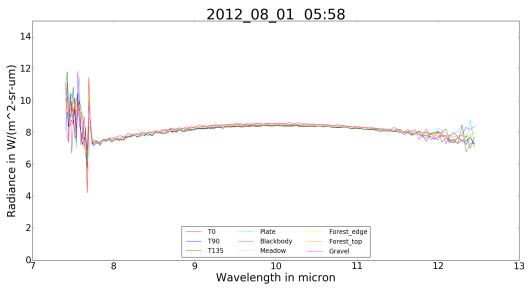

Figure 4.11: Average spectral radiance for nine materials in the scene observed on 1 Aug 2012 at 05:58, with heavy rain.

Figure 4.12: Band 10.1 μm from 1 Aug 2012, 05:58, calibrated radiance cube (histogram equalized to accentuate contrast).

ments through the atmosphere [5]. The sensor-reaching radiance was described through Equation 4.1

$$L(\lambda) = \epsilon B(T, \lambda)\tau_{atm} + (1 - \epsilon)L_d(\lambda) + L_a(\lambda) \tag{4.1}$$

where L(λ) was the sensor-reaching radiance, ϵ was the material emissivity, τ_{atm} was the atmospheric transmission, B(T,λ) was the blackbody radiance of the material, $L_d(\lambda)$ was the downwelling radiance and $L_a(\lambda)$ was the path radiance.

The input for MODTRAN generation are provided in Appendix B. The same parameters were run twice, once with spectral albedo (SALB) value of 0, and again with a SALB value of 1. Figure 4.13 illustrates a portion of the MODTRAN results for SALB=1. MODTRAN provided the results in

tape7 - /cis/masters/nj1520/MODTRAN2013/@armstrong

File Edit Search Preferences Shell Macro Windows

```
TS  2    2    2    1    2    2    2    2    2    2    1    0    0 293.2421.00
    1    1    1    0    0    0 23.00000   0.00000   0.00000   0.00000   0.21300
 -99.000 -99.000 -99.000 -99
 -99.00000 -99.00000 -99.00000  2.636178  0.000709 ! H2O & O3 COLUMNS [GM/CM2]
   36MIDLATITUDE SUMMER
   0.33900   0.21300 102.46230   0.58400   0.00513   0.00000    0
    1    2  121    0
  40.92800 -74.58100  14.83000 300.70752   8.00000   0.00000   0.00000   0.00000
       900      1260        1         1
    0   0    0.000  0    0.000  0    1.000
    FREQ  TOT TRANS  PTH THRML  THRML SCT  SURF EMIS   SOL SCAT  SING SCAT  GRND RFLT  DRCT RFLT  TOTAL RAD  REF SOL  SOL@OBS   DEPTH
  900.00 0.87730145 1.2411E-06            0.0000E+00 8.7994E-11 6.1369E-12 3.3990E-06 3.4118E-08 4.6402E-06 1.23E-07 1.45E-07   0.131
  901.00 0.87787408 1.2330E-06            0.0000E+00 8.8860E-11 6.1952E-12 3.3807E-06 3.4305E-08 4.6138E-06 1.24E-07 1.45E-07   0.130
  902.00 0.87704718 1.2395E-06            0.0000E+00 8.8605E-11 6.2048E-12 3.4005E-06 3.4186E-08 4.6401E-06 1.23E-07 1.45E-07   0.131
  903.00 0.87648427 1.2432E-06            0.0000E+00 8.8843E-11 6.2423E-12 3.4042E-06 3.4227E-08 4.6474E-06 1.23E-07 1.45E-07   0.132
  904.00 0.87851179 1.2200E-06            0.0000E+00 9.0463E-11 6.3245E-12 3.3589E-06 3.4577E-08 4.5790E-06 1.25E-07 1.46E-07   0.130
  905.00 0.87080085 1.2978E-06            0.0000E+00 8.6062E-11 6.1688E-12 3.5228E-06 3.3398E-08 4.8207E-06 1.20E-07 1.43E-07   0.138
  906.00 0.78976542 2.1248E-06            0.0000E+00 6.5234E-11 5.1291E-12 4.3056E-06 2.6968E-08 6.4305E-06 9.71E-08 1.21E-07   0.236
```

Figure 4.13: MODTRAN results for SALB=1 with the input provided as per Appendix B.

W/cm^{2}sr$\cdot cm^{-1}$. They were converted to W/m^{2}sr$\cdot\mu$m to compare with SPICE data.

MODTRAN provided τ_{atm}, $L_d(\lambda)$ and $L_a(\lambda)$ from Equation 4.1 where TOT TRANS is τ_{atm}, (GRND RFLT - DRCT RFLT) when SALB=1 is $L_d(\lambda)$, and PTH THRML when SALB=0 is $L_a(\lambda)$. Two assumptions were made to obtain B(T,λ) and ϵ. First, the blackbody radiance was calculated using Planck's law as described in Equation 4.2. For this, a temperature of 300K was assumed. The MODTRAN results for the path radiance, downwelled radiance, blackbody radiance at 300K and the transmission are provided in Figure 4.14.

$$Planck'sLaw = \frac{2hc^2}{\lambda^5 e^{\frac{hc}{\lambda kT}} - 1} \tag{4.2}$$

Second, a near-blackbody object from the scene (black canvas) was selected to compare with the MODTRAN results. Since a perfectly emissive material was unrealistic, an emissivity value of 0.97 was assumed for this ob-

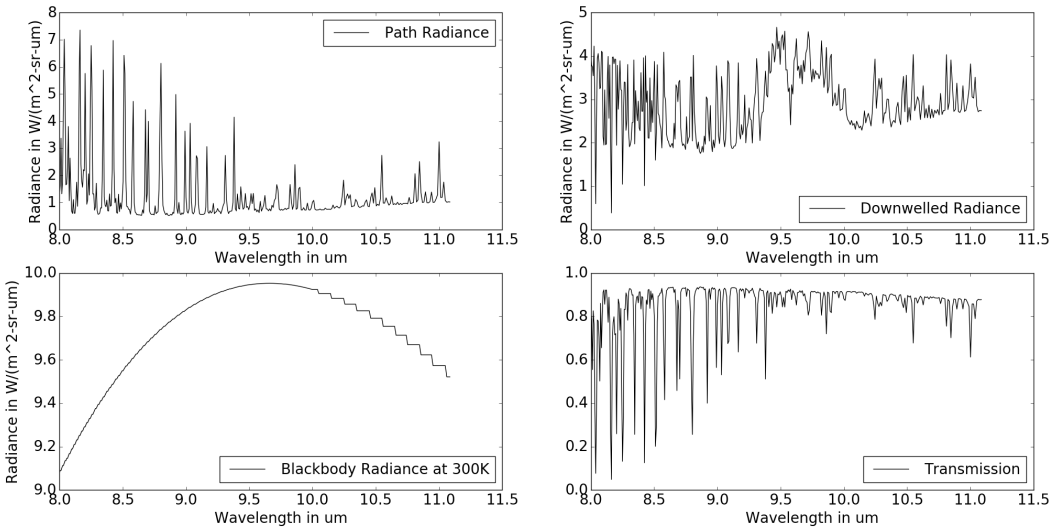

Figure 4.14: Top left: MODTRAN path radiance. Top right: MODTRAN downwelled radiance. Bottom left: Planck's law blackbody radiance at 300K. Bottom right: MODTRAN transmission. Results were obtained for a range of 8.00 to 11.09 μm using 349 spectral bands.

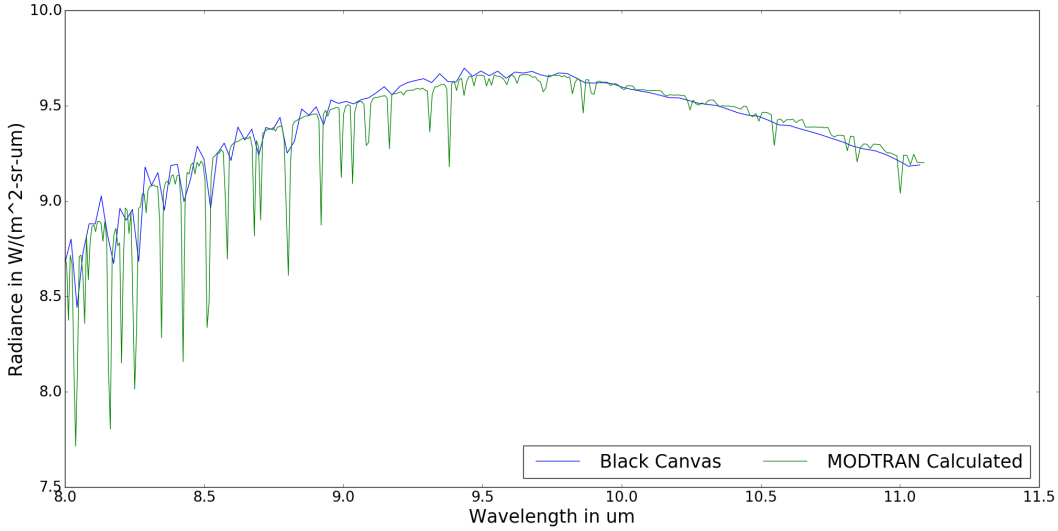

Figure 4.15: The sensor-reaching radiance using MODTRAN results in green and the spectral average of the black canvas from the scene in blue.

ject.

Using the MODTRAN results and the two assumptions, the sensor-reaching radiance for a near-blackbody was calculated using Equation 4.1. To compare with the SPICE data, the HSI corresponding to 11:58 from 1 May 2013 was selected. The spectral average of the black canvas and the results from Equation 4.1 were plotted against the wavelength and is shown in Figure 4.15.

Figure 4.15 validated the SPICE data since they were very close to the MODTRAN simulated data. It was noted that the MODTRAN data were much finer and incorporated the atmospheric absorption much better. This was due to MODTRAN having 349 spectral bands to cover approximately 8-11 μm, while the SPICE data had only 105 spectral bands to cover the same

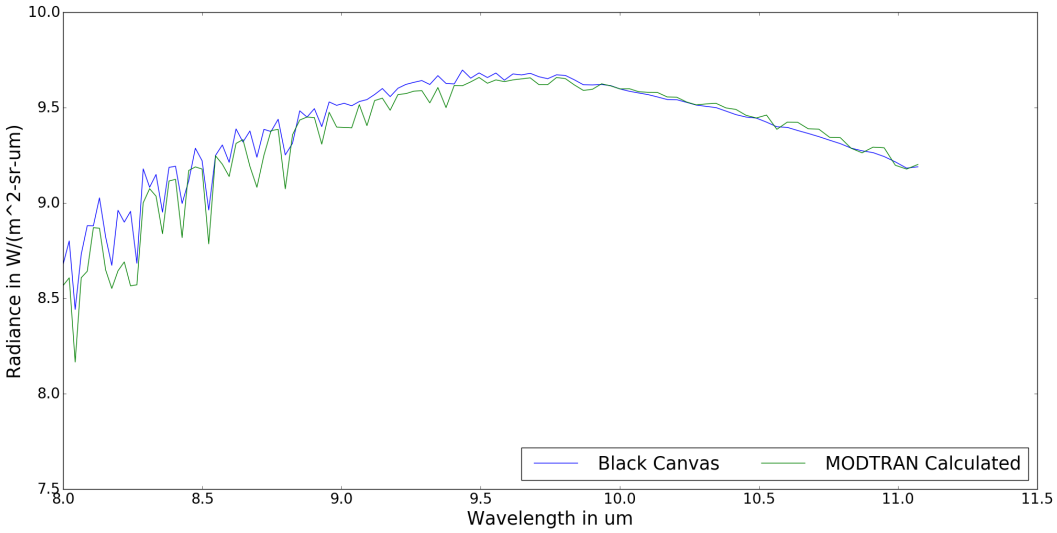

Figure 4.16: The sensor-reaching radiance using MODTRAN results in green and the spectral average of the black canvas from the scene in blue for 105 spectral bands.

spectral range. Yet, Figure 4.15 shows there were dips in the SPICE data for the same wavelengths as the MODTRAN results for atmospheric absorptions, just not as prominent.

MODTRAN results were produced with a spectral resolution of one wavenumber, whereas SPICE was collected with a spectral resolution of four wavenumbers. A responsivity of one was assumed for this calculation. With this assumption, the wavenumbers corresponding to the SPICE spectral bands were interpolated to the MODTRAN bands, and the adjacent four bands' values were averaged for each spectral band. The averaged MODTRAN results were plotted alongside the spectral average of the black canvas. This is displayed in Figure 4.16, where the atmospheric absorption is less prevalent.

4.3 Noise

The data provided by ARL were processed data cubes, and previous studies concluded that intrinsic system noise in the sensor was a minor to moderate concern compared to the atmospheric and environmental variation effects [34]. We characterized the instrument noise by calculating the difference standard deviation of a uniform object. For this method, we assumed the black panel to be locally uniform with negligible surrounding contribution.

4.3.1 Difference Standard Deviation

When a sensor is imaging a uniform area, it should result in the same value for all the pixels. If a subset of such uniform scene is subtracted from the same subset translated by one pixel to the right, the result should be zero, and any deviation may be attributed to sensor noise. The noise covariance can be approximated from the covariance of the neighboring pixel differences as per Equation 4.3 [37]

$$\Sigma_n \simeq \frac{1}{2}\Sigma_{\Delta n} \tag{4.3}$$

where Σ_n is the desired noise spectral covariance matrix and $\Sigma_{\Delta n}$ is the matrix formed by computing the spectral covariance of the pixel difference image.

Therefore, taking the standard deviation of the subset difference of the black panel and dividing by $\sqrt{2}$ should approximate the instrument noise.

Figures 4.17 and 4.18 provide the average black panel radiance provided

by ARL, along with noise as discussed in section 4.3.1 for midnight and noon timeframes. Telops specified that the typical NESR was <20 nW/cm^{2}sr·cm^{-1}. The green line is the specified NESR converted to the same units as the calculated noise.

The noise obtained from difference standard deviation on Figure 4.17 was very close to the NESR specified by Telops. We have to take into account that the NESR was calculated in a lab setting while the calculated noise was from real data, where there were many other factors influencing the results. In comparing the noise from the two timeframe (Figures 4.17 and 4.18), they behaved as expected. There was much higher noise in noon timeframe, because there was more signal during the day with higher temperature, therefore the photon noise will be larger.

4.3.2 Noise Correlation Coefficient Matrix

Depending on operating conditions, the noise associated with an imaging spectrometer can change drastically. The noise correlation coefficient matrix, the covariance between two bands normalized by the standard deviations in the two bands, is often used for visualization.

The correlation coefficient is represented by

$$\rho_{mn} = \frac{\sum_{q=1}^{N}[DC_m(q) - \overline{DC}_m][DC_n(q) - \overline{DC}_n]}{(N-1)\sigma_{mm}^{1/2}\sigma_{nn}^{1/2}} \tag{4.4}$$

where ρ_{mn} is the correlation coefficient between bands m and n, $DC_m(q)$ is

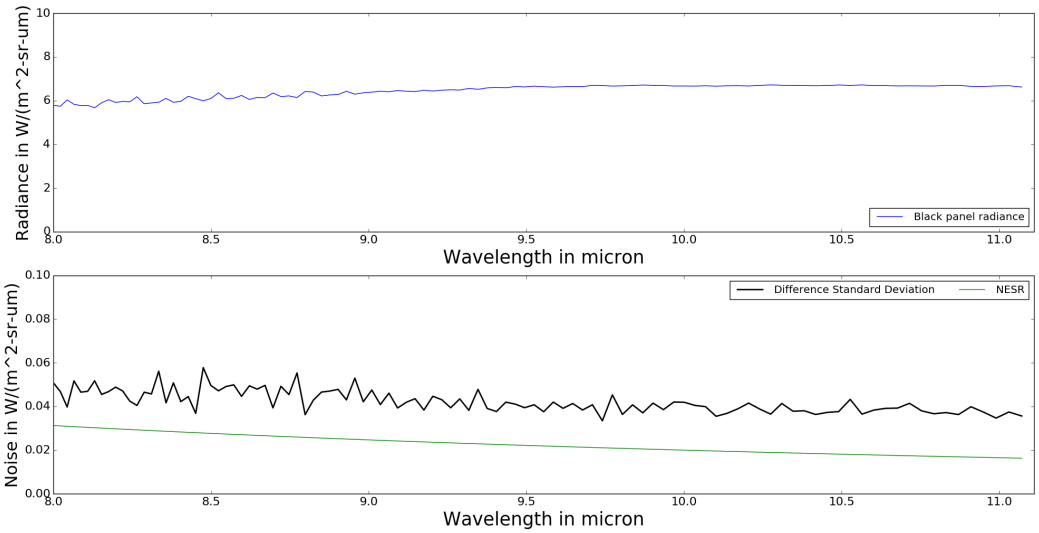

Figure 4.17: 01 May 2013, 23:58 black panel average radiance with 4.3.1 noise and provided NESR.

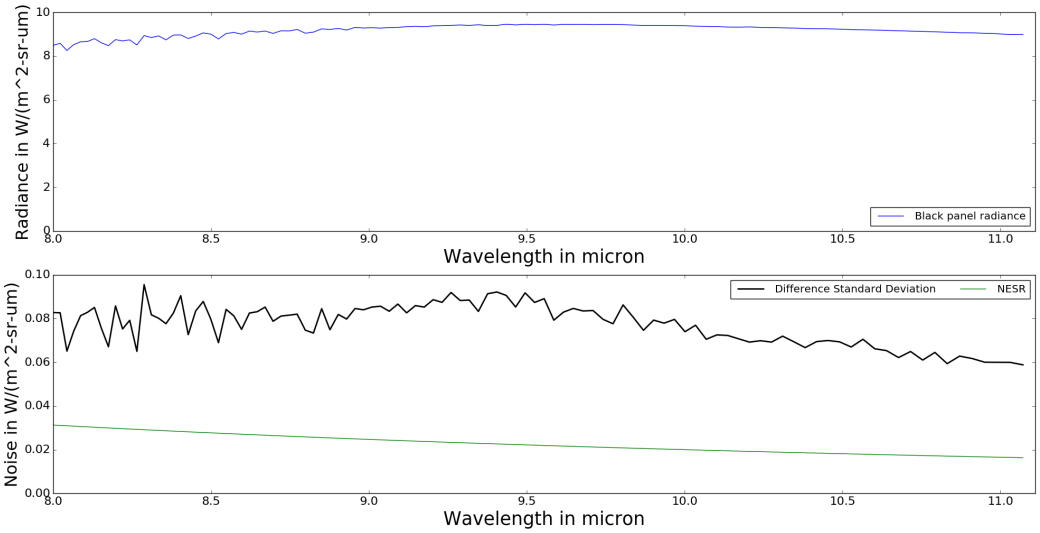

Figure 4.18: 01 May 2013, 11:58 black panel average radiance with 4.3.1 noise and provided NESR.

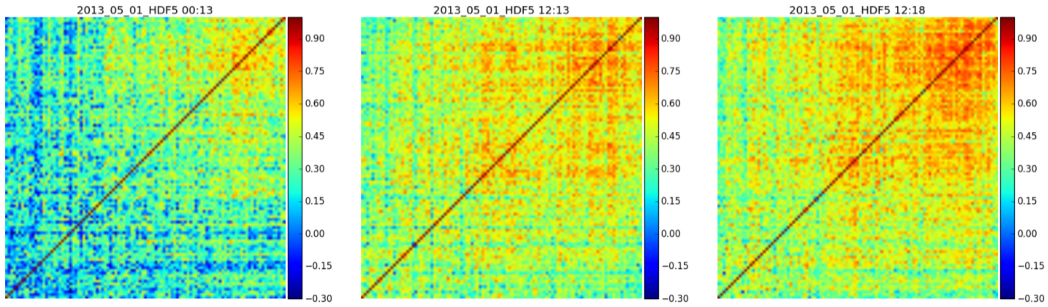

Figure 4.19: 01 May 2013, correlation coefficient matrix for 00:13 (left), 12:13 (center) and 12:18 (right)

the qth digital count from a noise sample of N pixels having mean $\overline{DC}_m$ and variance σ_{mm} in the mth band.

Equation 4.4 was used to compute the correlation coefficient matrix. Figure 4.19 depicts three correlation coefficient matrices for a difference subset in the black panel for three times on the same day. The difference subset image was obtained by taking the difference between a subset of the black panel and the same subset translated by one pixel to the right. It could be seen that even for a five minute acquisition time difference using the same sensor, the correlation matrices differ slightly.

4.4 Diurnal Data

4.4.1 Mean Variation Over Time

One of the significant characteristics of this dataset was its rich temporal content. The sensor had imaged the scene at approximately every 5 minutes while maintaining the same field of view. We could explore the temporal be-

haviour of several materials (manmade and natural) and compare them with each other. We expect the tanks to heat up during the day and cool down during the night with distinct variation between time of day. The skyplate should have the least variation since, unlike large pieces of metals, a thin sheet of aluminum will dissipate the heat absorbed very fast and since it is highly reflective, its radiance will vary with downwelled radiance. There should be slight differences between daytime radiance and nighttime radiance, but not as drastic to be expected of the tanks (the blackbody radiance of the tanks will increase since its temperature will increase as time progresses during the day, but the blackbody radiance of the white panel will remain relatively similar since its temperature will not rise as much). We also expect the four types of vegetation (near-trees, rear-trees, grass and bushes) to have similar trends.

The temporal mean variation of seven materials is shown in Figure 4.20 (Tank0, Gravel, White Panel, Black Panel, Grass, Near-trees and Rear-trees). For these materials, the average radiance at 10.0681μm for each material as per the masks in Figure 2.8 was plotted. It could be noted that day and night period were easily distinguishable even if an x-axis labeling the time of day was not present. During nighttime, all materials had low radiance and were very similar to each other. However, during daytime, select materials heated up and emitted higher radiance (notably the tank and the black panel). The aluminum panel behaved as expected, having very small variation for the course of the day. The slight increase during the middle of the day could be explained by the environment effect, since the air temperature ranged from

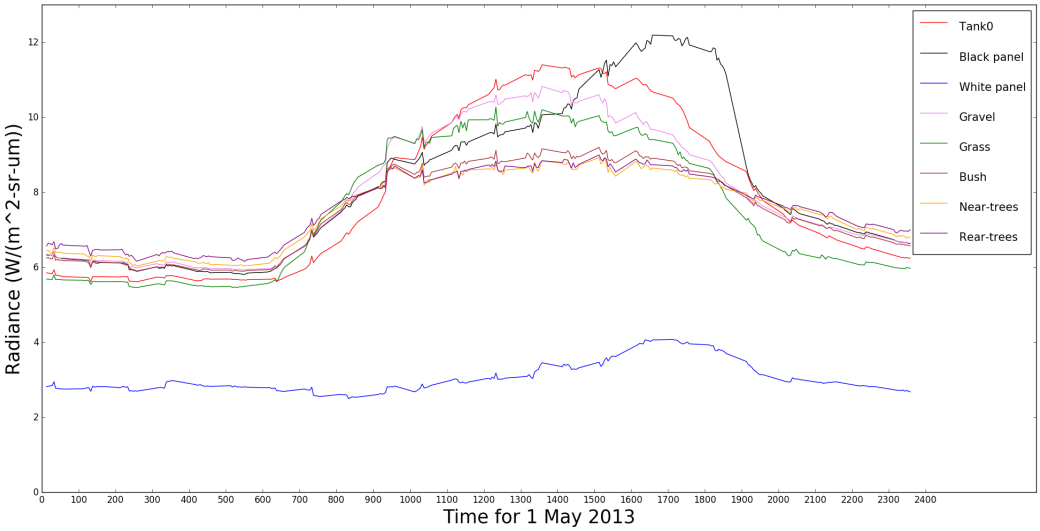

Figure 4.20: Temporal mean variation of eight materials for 24-hrs period using the band corresponding to 10.0681μm.

-1.9°C to 21°C between night and day. Despite being a very good reflector (as assumed to be a perfect reflector), the aluminum panel could have heated up during the day (in reality, the perfect reflector assumption is not 100% accurate), increasing its blackbody temperature, thus increasing the at-sensor radiance. An interesting phenomena was observed for the vegetation. The bush and the trees had similar trend during daytime, as one would expect due to them being all vegetation. However, the grass's trend was closer to the gravel than other vegetation. This could be due to soil effects (which indicate that each pixel in the mask is not definitively one material) as well as the grass was less exposed to the sky compared to the "taller" vegetation. This was even further observed during nighttime, when the radiance of the grass got much lower than any other vegetation.

4.4.2 Standard Deviation Variation Over Time

Similar to the temporal mean behaviour studied in Section 4.4.1, the temporal variance of each material could also be visually showcased. Since the variance is the square of the standard deviation, the trend will be comparatively the same when the standard deviation of a material's subset is plotted. In this plot, we expect very low variance in the white panel, but higher variance in "unsteady" material like the trees.

Even with a uniform material, the spatial variation may be influenced by surrounding materials causing edge effects. In order to minimize this influence, a smaller subsection of each material was used to calculate the radiance standard deviation. Note that the variation observed is a combination of instrument noise and spatial variability. Figure 4.21 shows that the white panel has minimal standard deviation. The true standard deviation of the white panel is expected to be smaller than what is shown in Figure 4.21 when we consider that the instrument noise is also a factor. Even if the white panel was considered a perfect reflector, there will be some variation observed by the sensor due to the path radiance, which will vary diurnally due to changes in atmospheric (air) temperature. The black panel followed the white panel, however, unlike the white panel, the temperature of the day did affect the standard deviation of the black panel. The material with the greatest standard deviation was the treed area, which was expected since it was the only "unsteady" material relative to the remaining "stationary" materials. In addition, the trees were not completely solid material. Despite only having a subset of

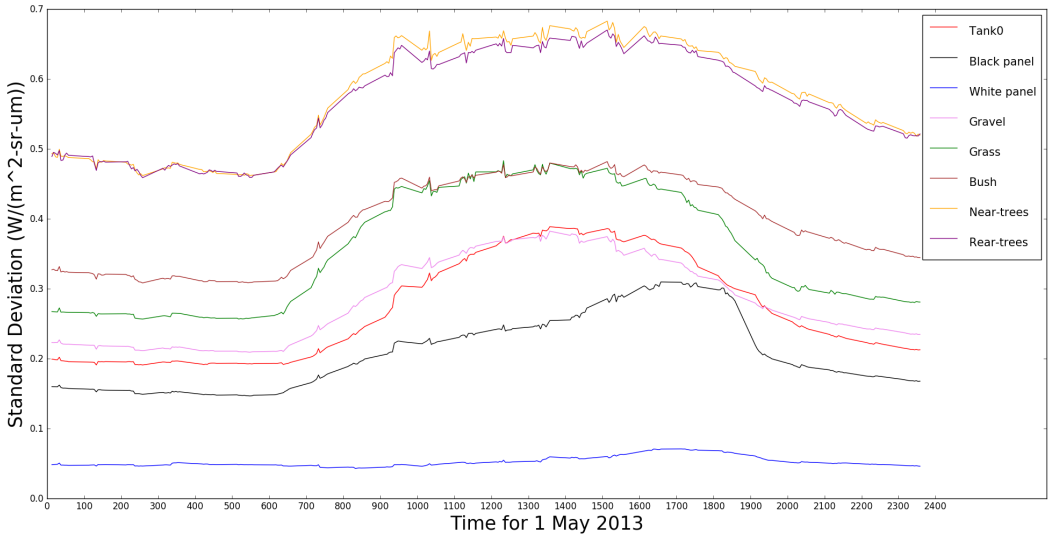

Figure 4.21: Temporal standard deviation variation of eight materials for 24-hrs using the band corresponding to 10.0681μm.

near-trees and rear-trees, there were "air gaps" that allowed "contamination" of other materials as well, which increased the standard deviation.

4.5 Spatial Variation

The spatial variation was investigated using the same materials. We compared the spatial variation of the two panels, the three tanks and the grass, for two distinct time frames. The range in radiance within each material were used to characterize the variation. The mask size for the black panel and the white panel were 8×13 and 7×11 pixels respectively. However, for this analysis, a subset of the mask (6×11 pixels for black panel, and 5×9 pixels for white panel) was used to limit adjacency effects.

4.5.1 Spatial Variation at Midnight

Figure 4.22 shows the spatial variation of two uniform targets (panels) and two semi-uniform targets (tanks and grass) for midnight time-frame. We expect minimal spatial variation within the two panels. The low variation (0.21 $W/m^2sr\cdot\mu m$) in the black panel cannot totally be considered spatial variation. It is the result of instrument noise as discussed in Section 4.3.1, combined with material variability and environment/adjacent material effects. The adjacency effect was better observed in the white panel. There was a larger variation in the white panel (0.35 $W/m^2sr\cdot\mu m$). This was after we omitted the edge pixels contributing to adjacent material effects (very low emissive aluminum surrounded by large emissive vegetation), yet the adjacency effect was still observed in the lower left of the panel. For a large surface area covering three tanks, the variation was only 0.9 $W/m^2sr\cdot\mu m$. A larger variation was observed in the grass (4 $W/m^2sr\cdot\mu m$).

4.5.2 Spatial Variation at Noon

Figure 4.23 shows the spatial variation of the same targets as for Figure 4.22 but for the noon time frame. There was greater variation within the uniform targets compared to Figure 4.22. This was expected since in reality, the panels did not heat-up uniformly (the upper portion of the black canvas absorbed more heat). The edge effects were more prominent in the white panel where the center of the panel was somewhat uniform while the top pixels and the left pixels had significant influence from the surrounding vegetation. We

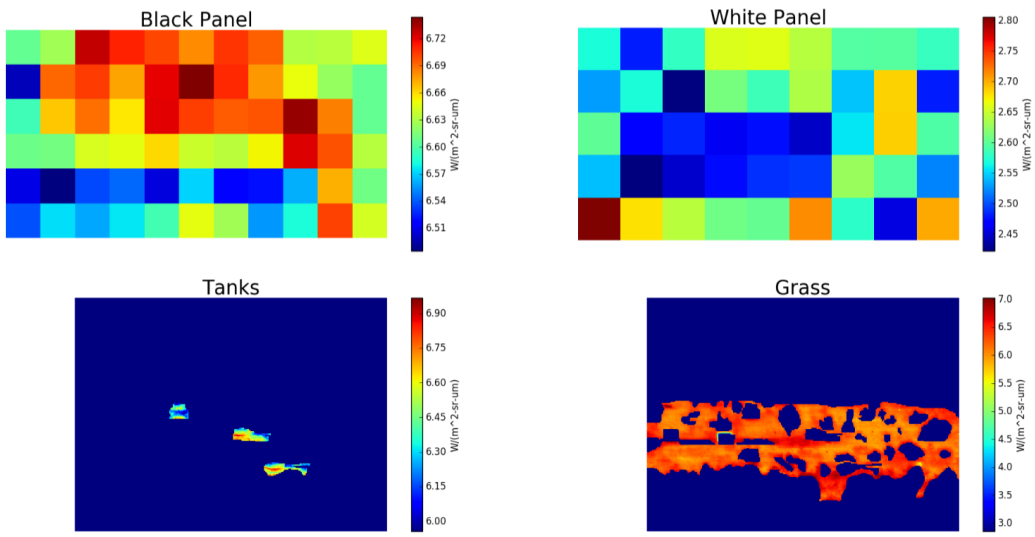

Figure 4.22: Spatial variation during midnight.

would expect greater spatial variation for the semi-uniform targets during noon since all parts of the tanks will not heat up equally. This was seen in lower-left portion of Figure 4.23, where the variation is 2.4 W/m^{2}sr$\cdot\mu$m. Despite best effort, the tank mask incorporated pixels that could be categorized as other materials due to "air gaps". As expected, the grass had the highest variation for this time-frame as well with 4.8 W/m^{2}sr$\cdot\mu$m.

The range of variation in the black panel was 0.9 W/m^{2}sr$\cdot\mu$m for noon and 0.21 W/m^{2}sr$\cdot\mu$m for midnight, while the range in the white panel was 0.56 W/m^{2}sr$\cdot\mu$m for noon and 0.35 W/m^{2}sr$\cdot\mu$m for midnight. This reflects our intuition that the black panel heated up with time, but not necessarily uniformly. Whereas, the aluminum panel was almost a perfect reflector and reflected the sky-radiance.

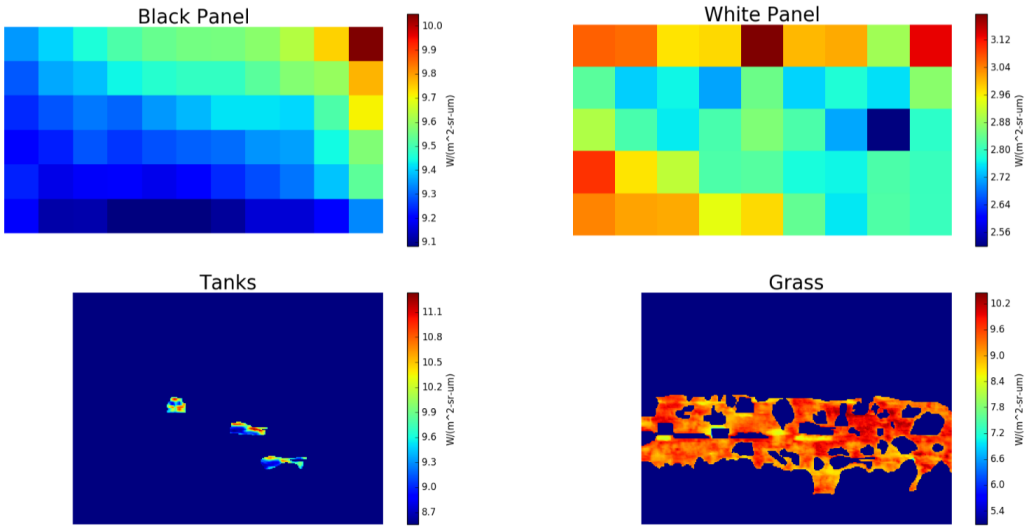

Figure 4.23: Spatial variation during noon.

Chapter 5

Scene Characterization

This chapter characterizes the scene using the temporal data. First, detection of the tanks was explored using three target detection methods. Next, the objects in the scene were classified using spectral and temporal signatures.

5.1 Tank Target Detection

Three signature matched detection algorithms were implemented on this dataset: Adaptive Coherence/Cosine Estimator (ACE) [19], Spectral Angle Mapper (SAM) [19], and Spectral Matched Filter (SMF) [19]. For these algorithms, the target spectral mean vector was calculated using Tank0. Both the target signature and the image data were in spectral radiance.

5.1.1 SAM

In SAM, the noise is assumed to be zero mean, white and normally distributed with an unknown variance σ^2. The variance is estimated by the square of the spectrum magnitude ($X^T X$). Under this assumption, the normalized projection is given:

$$r(X) = \frac{(S^T X)^2}{(S^T S)(X^T X)} \tag{5.1}$$

where S is the target spectrum and X is the pixel spectrum of the data.

The angle between the data and reference spectral vectors is calculated by taking the inverse cosine of the square root of Equation 5.1. Therefore, the detection statistic is:

$$r_{SAM}(X) = -cos^{-1}\left(\frac{(S^T X)^2}{(S^T S)(X^T X)}\right) \tag{5.2}$$

5.1.2 SMF

Due to zero-mean, white background clutter assumption, SAM's utility is limited. SMF addresses this limitation. One-sided SMF detection statistic was chosen to omit the detection of spectra less similar to the target spectrum than even the background mean. SMF can be applied with either global background sample statistics or local sample statistics. For this analysis, the global background will be used, which results in Equation 5.3

$$r_{SMF}(X) = (S - \widehat{\mu})^T \widehat{\Sigma}^{-1} (X - \widehat{\mu}) \tag{5.3}$$

where S is the target spectrum, $\widehat{\mu}$ is the global background average, $\widehat{\Sigma}^{-1}$ is the inverse covariance of the data and X is the data pixel spectrum under test.

5.1.3 ACE

ACE is described by:

$$r_{ACE}(X) = \frac{(S^T \widehat{\Sigma}^{-1} X)^2}{(S^T \widehat{\Sigma}^{-1} S)(X^T \widehat{\Sigma}^{-1} X)} \tag{5.4}$$

where S is the target spectrum, $\widehat{\Sigma}^{-1}$ is the inverse covariance of the data and X is the pixel spectrum of the data.

5.1.4 Tank Target Detection Results

Temporal target detection was attempted using the dataset. Temporal target detection in this case is defined as using a target's spectral signature from one period of time to detect the target in different time periods (full diurnal cycle). ACE, SAM, and SMF were implemented for two-scenarios to detect a target, and the area under the receiver operating characteristic (ROC) curve was used to quantify the rate of detection. For both scenarios, the average of Tank0 was used as the target spectrum and all three tanks were identified as "true" targets. Only 50 bands (9-10.5μm) out of 165 bands were used for target detection. For scenario one, target spectra were obtained from a noon cube (11:58) and a midnight cube (23:58) from 1 May 2013. They were used to detect the tanks from the same day data cubes. For scenario two, the same target spectrum from 1 May was used to detect the tanks on 2 May 2013 data cubes.

Figure 5.1 displays the results for scenario one.

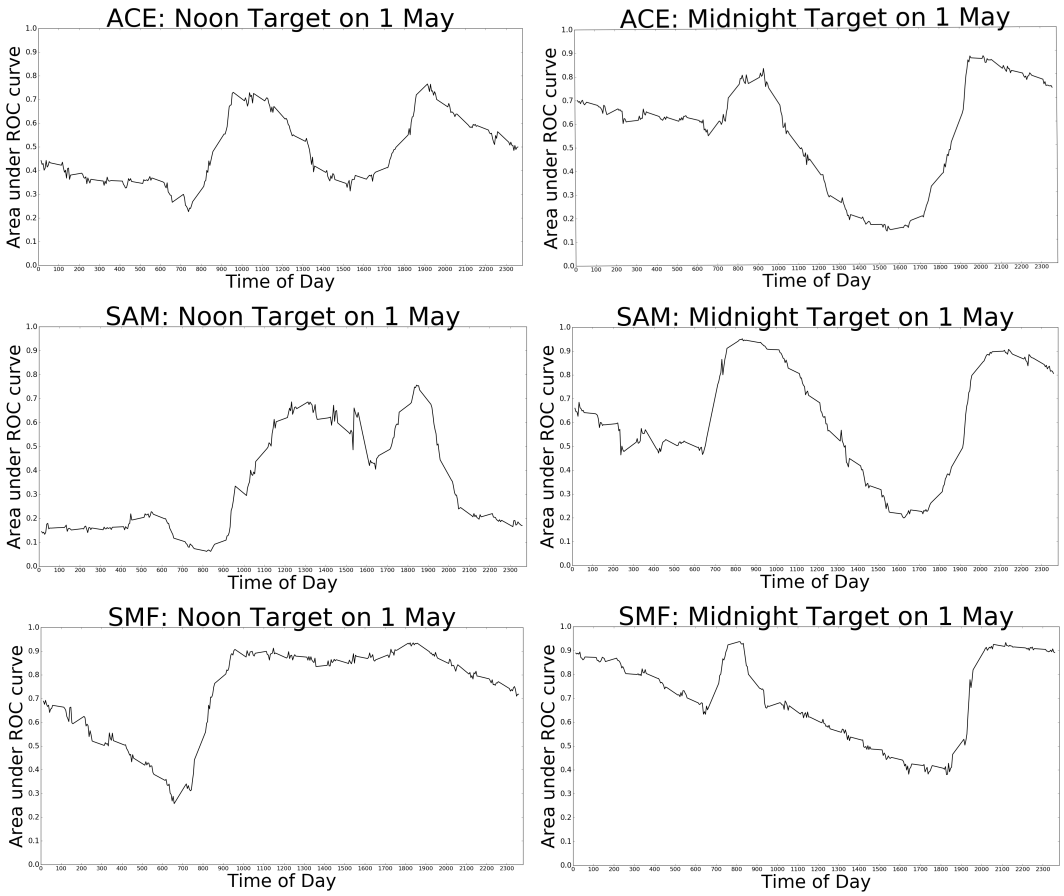

Figure 5.1: The area under the ROC curve for three detection algorithms are plotted against time of day for 1 May 2012. Left (top-down): ACE, SAM, and SMF for noon. Right (top-down): ACE, SAM, and SMF for midnight

Figure 5.2 displays the results for scenario two.

If we assumed that a threshold higher than 0.8 area under the ROC curve was a good indicator of target detection, SMF produced better results for both noon and midnight target spectra. One possible explanation for SMF yielding better results could be that, unlike ACE and SAM, SMF also used the background sample statistics in addition to the inverse covariance of the data. The percentage of detection in a day for both time-frames by each method is detailed in Table 5.1.

Table 5.1: Time index percentage of area under the curve greater than 0.8 (noon/midnight).

	ACE	**SAM**	**SMF**
1 May 2013	0.0% / 13.3%	0.0% / 32.5%	52.1% / 40.0%
2 May 2013	4.2% / 25.6%	0.0% / 35.8%	52.9% / 39.6%

It was noticed that the noon target spectrum produced higher detection rate for daytime compared to nighttime. However, when the midnight spectrum was used, daytime sometimes produced higher detection rate than nighttime. One possible phyical explanation for this phenomena could be that during daytime, high cloud presence blocked most of the sun, preventing the man-made materials to heat up. To verify this theory, the relative humidity was plotted for the full diurnal cycles of 1 and 2 May 2013 as shown in Figures 5.3 and 5.4. However, it was seen that the relative humidity during the day was low for both days, which implied that cloud formation was not present. Therefore, high cloud concentration was not the reason for the midnight spectrum yielding higher target detection rate for daytime data. On the other

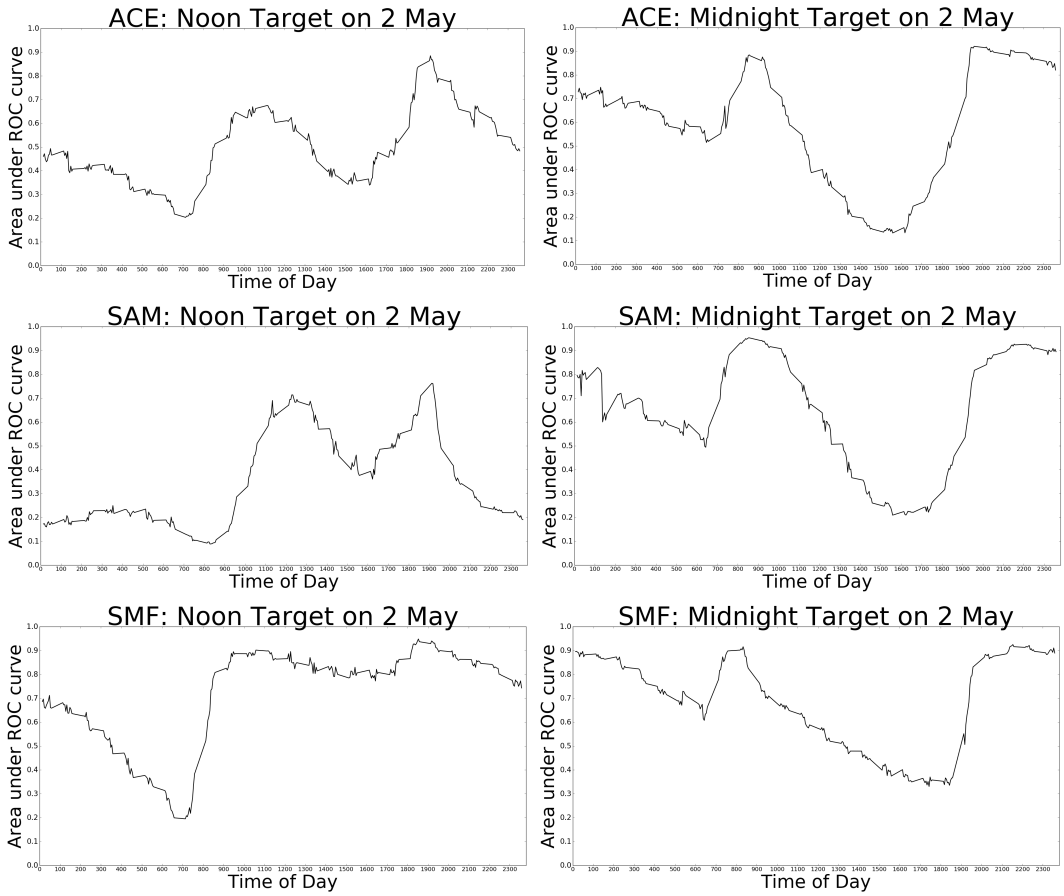

Figure 5.2: The area under the ROC curve for three detection algorithms are plotted against time of day for 2 May 2012. Left (top-down): ACE, SAM, and SMF for noon. Right (top-down): ACE, SAM, and SMF for midnight

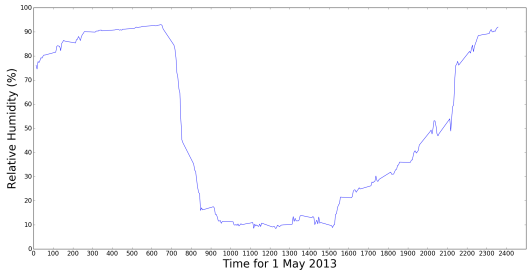

Figure 5.3: Relative humidity for 1 May 2013 diurnal cycle.

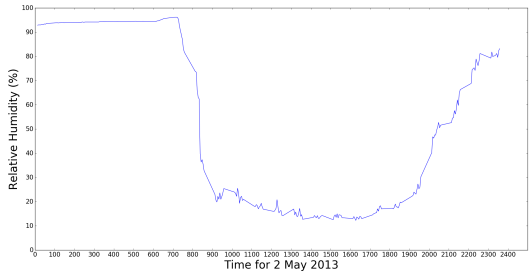

Figure 5.4: Relative humidity for 2 May 2013 diurnal cycle.

hand, Figures 5.3 and 5.4 emphasize the fact that in terms of meteorological comparison, 1 and 2 May 2013 are similar days.

It was also noticeable that the plots in Figure 5.1 were very similar to plots in Figure 5.2. This indicate that targets could be detected on data spanning multiple days for time frames approximately similar to when the target spectra was obtained (given that overall meteorological conditions were comparable).

5.2 Hyper Temporal Classification

The customary way to classify HSI is to use spectral signature, mostly from material emissivity or reflectance. This is done so because the spectral signatures between materials are often different, thus providing a good classification map. The greatest asset of the SPICE dataset was its temporal data. With this dataset, a rather unique classification of materials was attempted: use the temporal signature from the radiance data. Two drastically different timeframes, noon and midnight, were selected for spectral classification. The

spectral and temporal image classifications were compared and quantified to describe their performance.

5.2.1 Data Cubes

The first step was to create a hyper temporal image that could be used for image classification (this cube will have spatial and temporal data). Hyper temporal in this case was defined as continuously imaging a scene approximately every 5 minutes. Two different methods were explored to accomplish this task; single band and broadband temporal images. To describe the two methods, the full diurnal data from 1 May 2013 is used, which contained 240 usable HSI (224 $\times$ 300 pixels $\times$ 105 bands spanning 8.00075 μm to 11.0712 μm).

1. Single Band Temporal Image

   For this method, select a high atmospherically transmissive band among the 105 bands (the band corresponding to 10.1 μm). This band will be extracted from each of the 240 HSI and concatenated to make a hypertemporal image consisting of 224 $\times$ 300 pixels $\times$ 240 time samples depicting the 24-hour period of 1 May 2013.

2. Broadband Temporal Image

   In this method, instead of extracting one single band from the HSI, the average of all 105 bands will be calculated to simulate broadband sensor images. This in theory, should increase the signal to noise ratio, thus

producing better classification results. Similar to the previous method, the resulting hypertemporal image will be 224 × 300 pixels × 240 time samples depicting the 24-hour period of 1 May 2013.

The spectral cube will have 105 dimensions while the temporal cube will have 240 dimensions. In order to compare with similar dimensionality, the temporal broadband cube will be used in two formats:

- 240-Dimensions

  As mentioned in Part 2, the full 240 time samples will be used to classify the materials.

- 120-Dimensions

  To compare with similar dimensionality with the spectral cube of 105 bands, every second time sample from the 240 time samples will be collected, thus forming a cube consisting of 224 × 300 pixels × 120 time samples. The results between the 120 time samples and 240 time samples cubes will also be compared to analyze the differences.

In total, four different data cubes will be used for classification, one spectral and three temporal.

1. Spectral Noon

   The cube corresponding to noon timeframe from 1 May 2013 and 2 May 2013.

2. Temporal 10.1um

   The band corresponding to 10.1 μm will be concatenated from 1 May 2013 and 2 May 2013.

3. Temporal Broadband 240 time samples

   The average of 105 bands will be concatenated from 1 May 2013 and 2 May 2013.

4. Temporal Broadband 120 time samples

   The average of 105 bands will be concatenated from 1 May 2013 and 2 May 2013, and every 2nd time sample will be extracted to form a cube with 120 time samples.

For all these cubes, either the target signature from 1 May 2013 will be tested on 2 May 2013 data, or training will be done on 1 May 2013 and tested on 2 May 2013 data.

5.2.2 Reference Map

The ground truth was created using ENVI. The ground truth class map was similar to Figure 2.8, but included variations. The differences between Figure 2.8 and the ground truth class maps were the absence of miscellaneous background pixels and the combination of different classes into one class as described in Figure 5.5.

Figure 5.5 left classifies all vegetation under one class. Figure 5.5 center classifies rear-trees, near-trees and bushes as one class, and grass as a different

Figure 5.5: Ground truth class maps. Left: 7 Classes. Center: 8 Classes. Right: 10 Classes.(Tank0 [blue], Tank90 [light blue], Tank135 [sky blue], Black panel [navy blue], Skyplate [dark yellow], Gravel [aqua], Grass [orange], Bush [yellow], Near-trees [red], Rear-trees [maroon])

class. Figure 5.5 right classifies rear-trees, near-trees, bushes and grass as four different classes.

Unsupervised and supervised classification methods were used to classify the spectral and temporal cubes. K-Means was used as the unsupervised classification method. Three different supervised classification methods were used to classify the hyper temporal images: Euclidean distance, SAM, and Support Vector Machine (SVM).

5.2.3 Euclidean Distance

The Euclidean distance is defined using the following formula.

$$r(\mathbf{S_c}, \mathbf{X}) = \sqrt{\sum_{i=1}^{n} (S_i - X_i)^2} \tag{5.5}$$

where S is the target temporal signature, $_{\mathbf{c}}$ is the class index, X is the pixel temporal data, and n is the number of bands (for 1 May 2017, n=240). S is

retrieved by calculating the average material value per band using the material mask shown in Figure 5.5 for the different variations of the material class studied.

The euclidean distance between each pixel signature and all target signatures will be calculated. Each pixel will be classified to the target temporal signature yielding the lowest euclidean distance.

5.2.4 Spectral Angle Mapper

Equation 5.2 was used to calculate the angle between the pixel data and the target signature. The target class yielding the lowest angle was assigned to the pixel.

5.2.5 Support Vector Machine

Support Vector Machine (SVM) is a supervised machine learning method that can be used for classification that is effective in high dimensional spaces. Different kernel function can be specified in SVM. We used two Support Vector Classification (SVC) kernels, Linear and Radial Basis Function (RBF). The linear kernel is much faster, however the non-linear (RBF) kernel typically provides a better predictive performance. A higher classification accuracy is expected from the RBF SVC compared to the linear SVC [20]. A sample example of linear and RBF classification is provided in Figure 5.6, which was modified from a Python tutorial website [8].

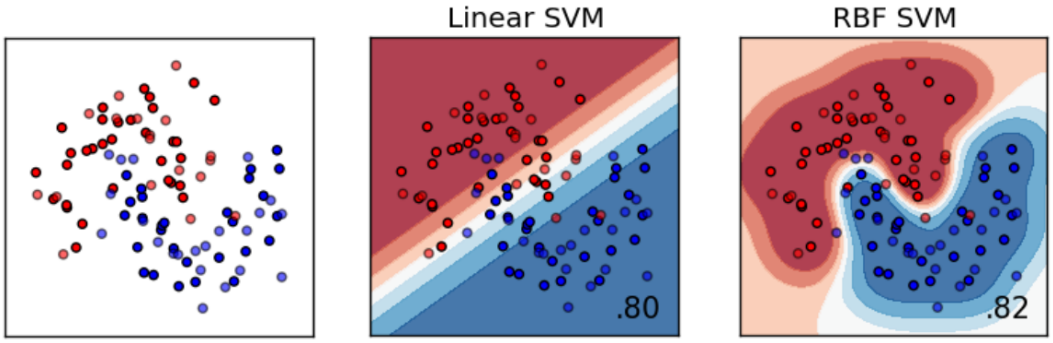

Figure 5.6: Classification of random points into two classes. Left: Random points. Center: Linear SVM classification result. Right: RBF SVM classification result. [8]

5.2.6 Classification Results Naming Convention

Four classification methods were applied on four image cubes. In order to minimize confusion, the classification method and the image cube the method being applied on will be amalgamated when discussing the results. Table 5.2 provides the names that will be used when discussing the results. The columns are the four classification methods (Euclidean, SAM, Linear SVC and RBF SVC). The rows are the four image cube types being classified (one spectral and three temporal cubes).

5.2.7 Comparison Metrics

Once the classification image was retrieved using the various methods described, three metrics were used to assess their performance and to compare with the different classification methods. The metrics were weighted accuracy, non-weighted accuracy and kappa, all calculated from the confusion matrix

Table 5.2: Classification Results Tabulation

	Euclidean	**SAM**	**Linear SVC**	**RBF SVC**
Spectral Noon	Euclidean-S	SAM-S	Linear-S	RBF-S
Temporal 10.1um	Euclidean-10.1	SAM-10.1	Linear-10.1	RBF-10.1
Temporal Broadband 240 time samples	Euclidean-240	SAM-240	Linear-240	RBF-240
Temporal Broadband 120 time samples	Euclidean-120	SAM-120	Linear-120	RBF-120

derived from the ground truth classification image and the classification result. To facilitate the explanation of the metrics, a sample confusion matrix is shown in Figure 5.7.

Weighted Accuracy

The weighted accuracy is calculated by summing the true positive of each class (diagonal values from the confusion matrix) and dividing by the total number of image pixels as shown in Equation 5.6.

$$Accuracy_{weighted} = \frac{\sum_{i=1}^{n} TP_i}{TOT} \tag{5.6}$$

where n is the number of classes, TP is the class true positive, and TOT is the total number of pixels in the classification image (sum of the confusion matrix).

Non-weighted Accuracy

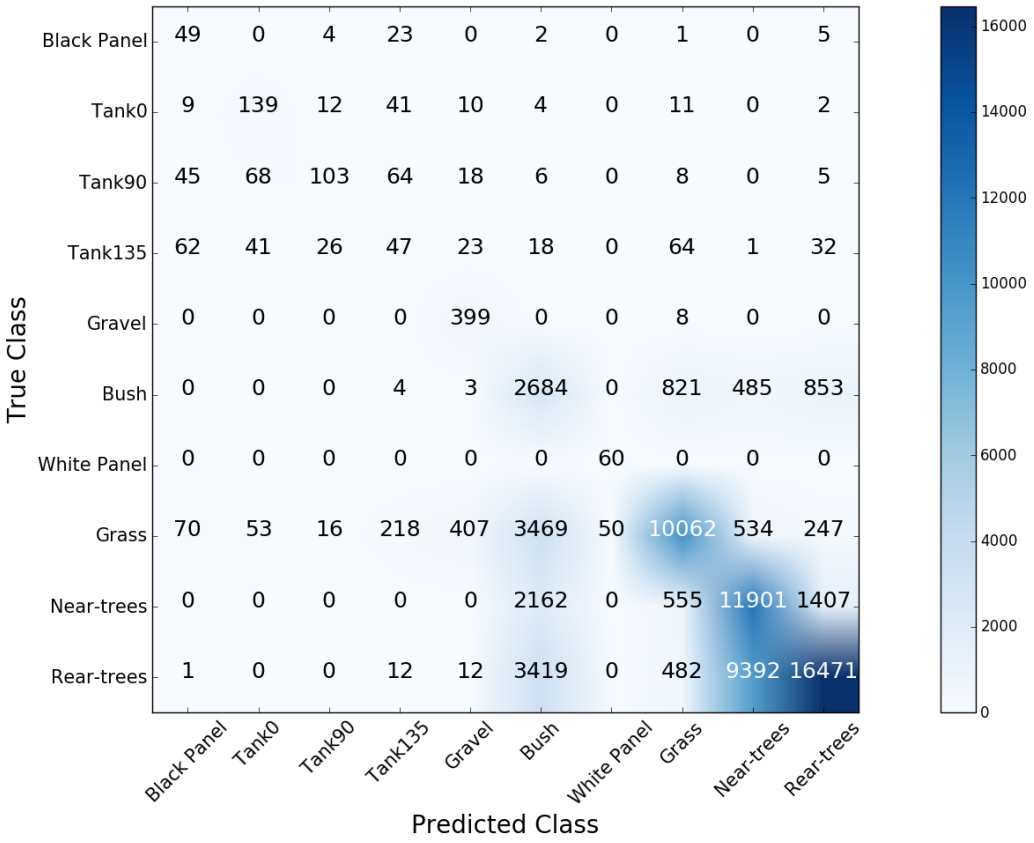

Figure 5.7: Euclidean distance result classification image's confusion matrix (target signature: 1 May 2013, testing cube: 1 May 2013)

The non-weighted accuracy is calculated by averaging the per-class accuracy as shown in Equation 5.7.

$$Accuracy_{non-weighted} = \frac{\sum_{i=1}^{n} \frac{TP_i}{GT_i}}{n} \tag{5.7}$$

where n is the number of classes, TP is the class true positive, and GT is the per-class ground truth.

Kappa

Kappa (κ) quantifies how well a classifier performed compared to how well it would have performed simply by chance. It takes into account the observed accuracy and the expected accuracy. In this case, the observed accuracy is the weighted accuracy as described earlier. Expected accuracy is calculated using Equation 5.8.

$$Accuracy_{expected} = \frac{\sum_{i=1}^{n} (\frac{TC_i \times PC_i}{TOT})}{TOT} \tag{5.8}$$

where n is the number of classes, TC is the true value per class (horizontal sum per class from Figure 5.7), PC is the predicted value per class (vertical sum per class from Figure 5.7), and TOT is the total number of pixels in the classification image (sum of the confusion matrix).

κ is calculated using Equation 5.9.

$$\kappa = \frac{Acc_{obs} - Acc_{exp}}{1 - Acc_{exp}} \tag{5.9}$$

where Acc_{obs} is the observed accuracy, and Acc_{exp} is the expected accuracy (weighted accuracy).

5.2.8 Unsupervised Classification Results

K-Means classification, an unsupervised classification method, was applied on the data from 1 May 2013 to see the difference in performance between the spectral and temporal data. For the spectral data, a HSI corresponding to noon timeframe and another HSI corresponding to midnight timeframe were selected. For the temporal data, the 10.1 μm band was concatenated to form the hyper temporal image. The K-Means algorithm from ENVI was run multiple times with different K values. The results for K=5 and K=10 runs are displayed in Figures 5.8 to 5.13.

Applying K-Means classification method, the temporal data differentiated the man-made objects better than the spectral data. Figure 5.12 classified the man-made objects with two colors, aqua (tanks and black panel) and red (skyplate). Figure 5.13 classified the man-made objects in orange (tanks and black panel) and red (skyplate). Both figures also classified the gravel in the same class as the tanks. And in both cases, these materials were explicitly different from the surrounding vegetation. On the other hand, the spectral data did not have clear distinction between these objects and the surrounding vegetation as displayed in Figures 5.8 to 5.11.

In order to quantify the spectral and temporal unsupervised classification results, the class corresponding to the tanks were analyzed. An image

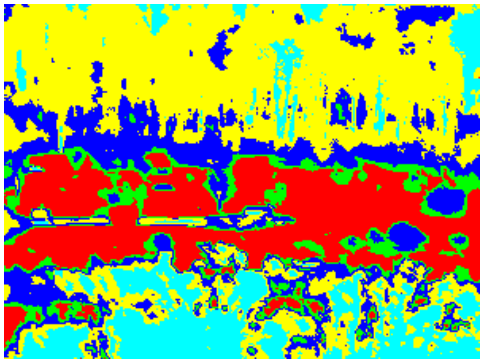

Figure 5.8: K-Means Classification (K=5), 1 May midnight HSI

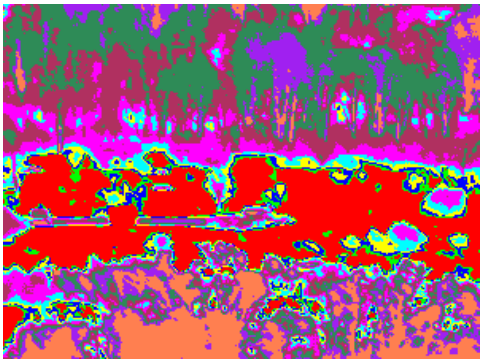

Figure 5.9: K-Means Classification (K=10), 1 May midnight HSI

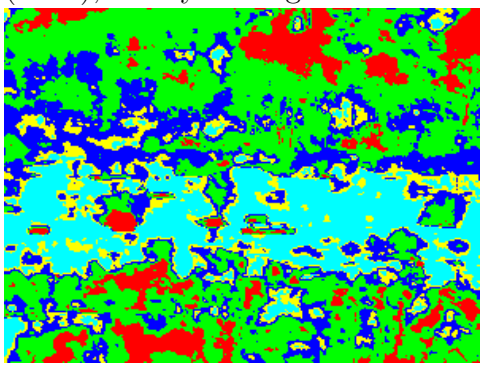

Figure 5.10: K-Means Classification (K=5), 1 May noon HSI

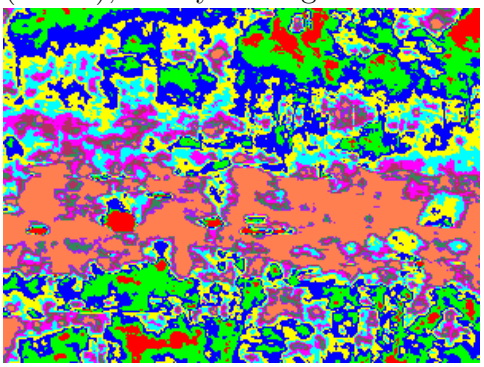

Figure 5.11: K-Means Classification (K=10), 1 May noon HSI

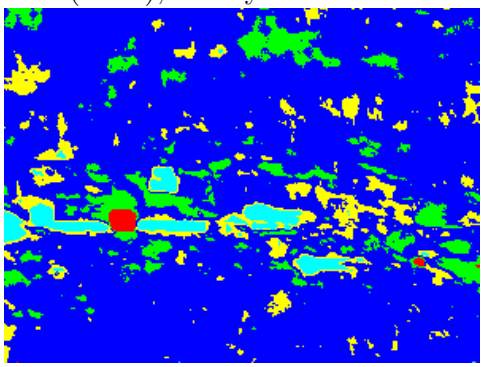

Figure 5.12: K-Means Classification (K=5), 1 May temporal cube

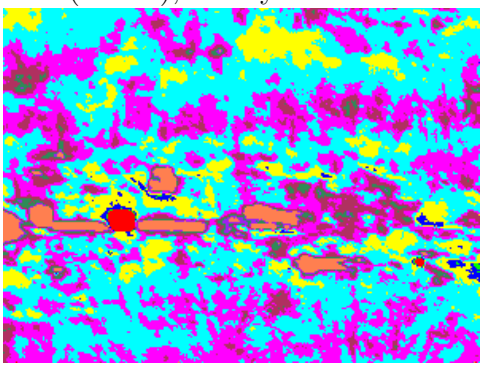

Figure 5.13: K-Means Classification (K=10), 1 May temporal cube

Table 5.3: K-Means classification rates for 1 May 2013 spectral and temporal data.

	Noon HSI		**Midnight HSI**		**Temporal**	
	K=5	K=10	K=5	K=10	K=5	K=10
Accuracy (%)	83.2	85.2	79.9	81.8	97.9	98.2
True Positive (%)	5.0	5.5	2.3	2.2	35.8	37.8
False Positive (%)	0.49	0.53	1.03	1.07	0.32	0.41
Precision (%)	67.9	65.1	35.3	30.9	75.3	68.7

containing only one class (i.e. aqua for K=5 and orange for K=10 for the temporal data) was created with everything else being background. These images were compared to a reference class map containing only the three tanks. The results are displayed in Table 5.3. The accuracy rates are high due to the high number of background pixels. The precision rates are good indicators for temporal data, especially when all three tanks are well defined (in addition to the gravel and black panel).

5.2.9 Supervised Classification Results

7 Class - Train/Test on 1 May 2013

Unsupervised image classification yielded better image classification when using hypertemporal data than hyperspectral data. The four supervised classification methods were tested on the same data as Section 5.2.8 (training and testing conducted on 1 May 2013) using 7-class ground truth class map. Being consistent with Section 5.2.8, hypertemporal data outperformed hyperspectral data in image classification as observed in Figures 5.14 and 5.15. The two SVM methods yielded a weighted accuracy of over 99% for seven out of possible eight scenarios, however Linear-240 and Linear-120 obtained the highest weighted accuracy of 99.36%. Linear-10.1 obtained the highest non-weighted accuracy with 57%, while all both SVM methods yielded a Kappa value of 0.99. Although the hypertemporal data outperformed hyperspectral data when using the same data for training and testing, their differences were not as drastic as observed in Section 5.2.8.

The remainder of the supervised classification results were obtained using 1 May 2013 data for training and 2 May 2013 data for testing.

7 Class

The scene was segmented into seven classes (Tank0, Tank90, Tank135, black panel, skyplate, gravel and vegetation) as displayed in the left portion of Figure 5.5. Qualitatively (visual inspection), Linear-S provided the best result. Quantitatively, Linear-S also had the highest weighted accuracy (99%) and

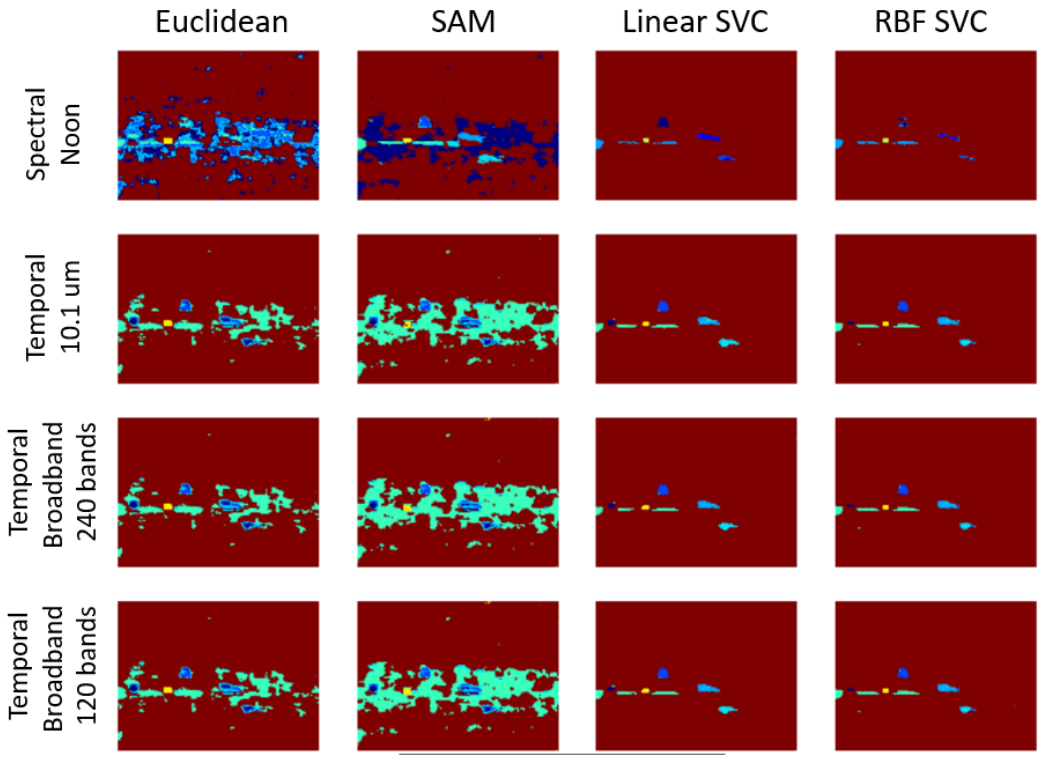

Figure 5.14: Classification results for 7-class (training and testing on 1 May 2013)

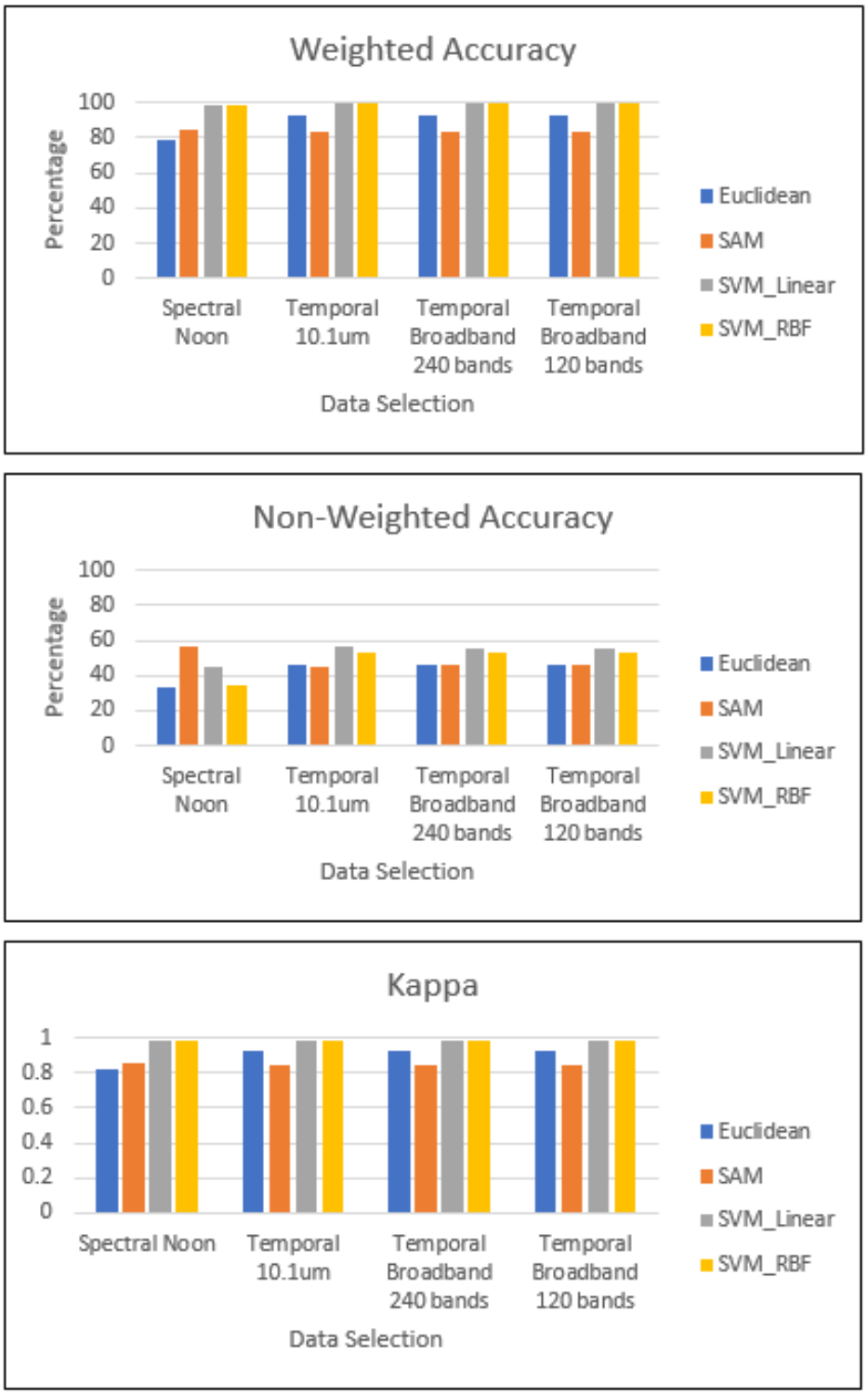

Figure 5.15: Weighted accuracy, non-weighted accuracy and kappa for 7-class classification (training and testing on 1 May 2013).

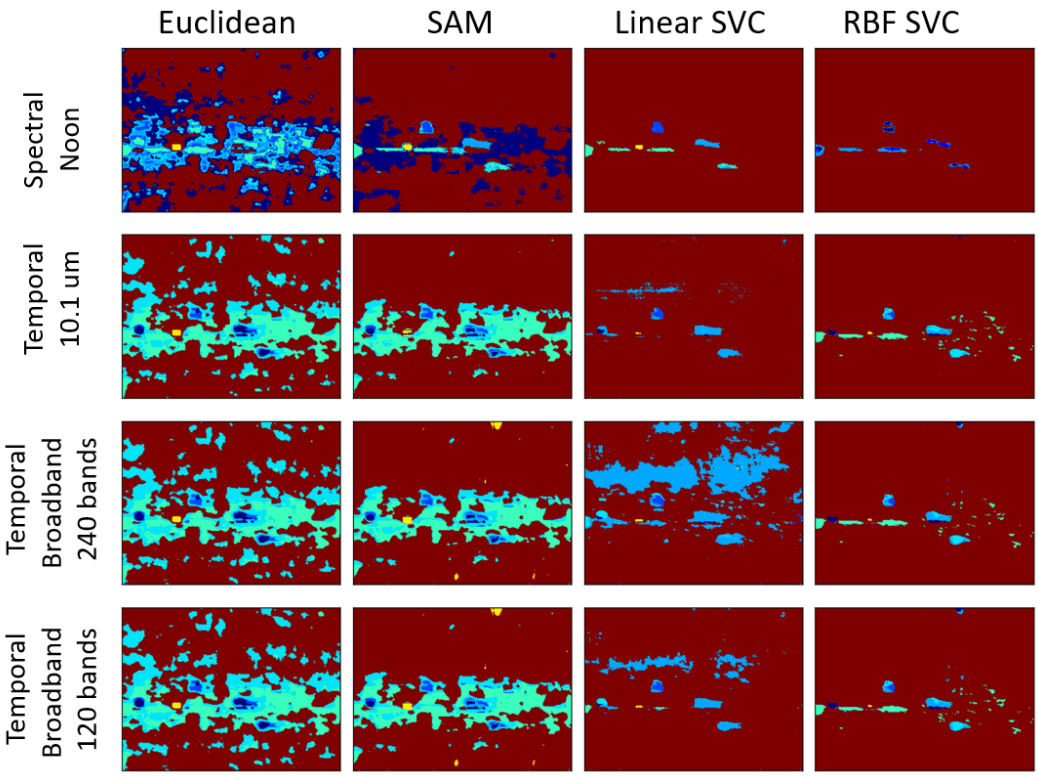

Figure 5.16: Classification results for 7-class

the highest κ (0.99), while SAM-120s had the highest non-weighted accuracy (48.84%).

8 Class

The scene was segmented into eight classes (Tank0, Tank90, Tank135, black panel, skyplate, gravel, grass and vegetation) as displayed in the center portion of Figure 5.5. Here, the low level vegetation (grass) was differentiated with higher level vegetation. Qualitatively, SAM-S displayed the best result. Quantitatively, Linear-S had the highest weighted accuracy (88.42%)

Figure 5.17: Weighted accuracy, non-weighted accuracy and kappa for 7-class classification.

and the highest κ (0.91), while SAM-S has the highest non-weighted accuracy (62.82%).

It is interesting to note that the RBF-10.1, RBF-120 and RBF-240 yielded results very similar to the 7-class segmentation, while RBF-10.1 classified all vegetation as grass and the broadbands classified all grass as vegetation as well. In the temporal cubes for both Euclidean and SAM classification methods, it was noticeable that a lot of the grass pixels were classified as gravel. This repeated the phenomena observed in Figure 4.20 where the grass shared a similar temporal signature to gravel compared to the other vegetation.

10 Class

The scene was segmented into ten classes (Tank0, Tank90, Tank135, black panel, skyplate, gravel, grass, bush, near-trees and rear-trees) as displayed in the right portion of Figure 5.5. For this segmentation, the higher level vegetation were separated into three classes (bush, near-trees and rear-trees). Visually, RBF-10.1 yielded the best results. Quantitatively, RBF-S had the highest weighted accuracy (70.25%) and κ (0.56) while SAM-S had the highest non-weighted accuracy (68.77%).

The unsupervised classification method seemed to indicate that a better classification could be achieved by using the temporal signature instead of the spectral signature as observed in Figures 5.8 to 5.13. This was supported by supervised classification methods when using the same data for training and testing as observed in Figures 5.14 and 5.15. However, different results

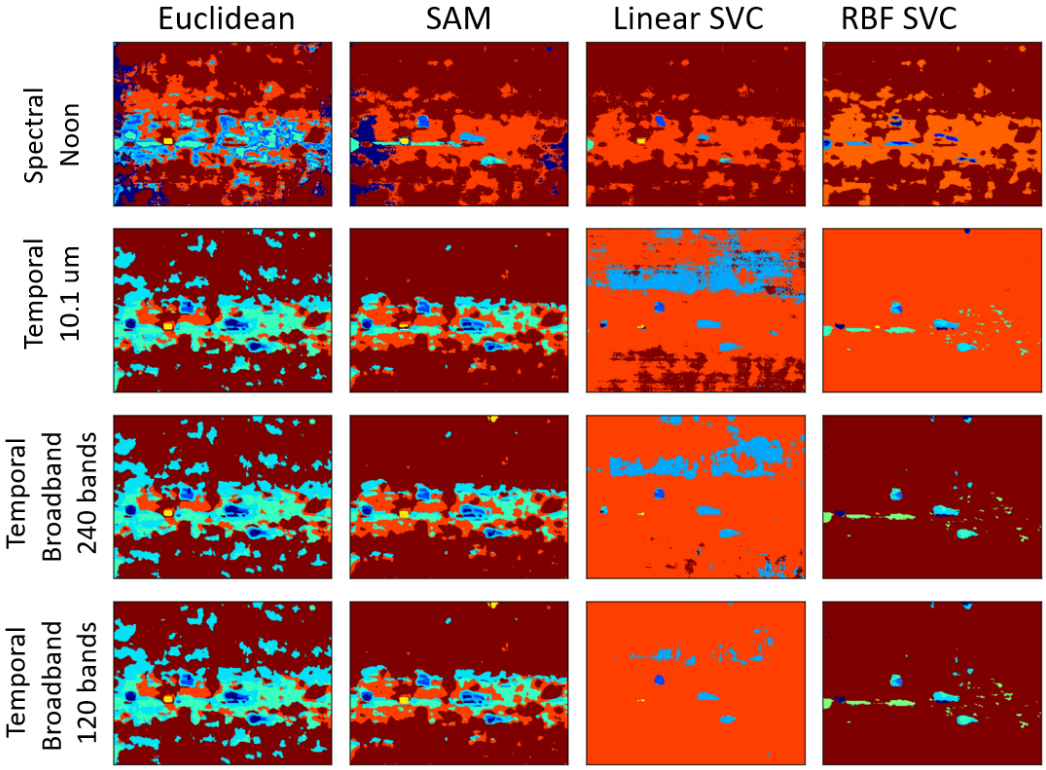

Figure 5.18: Classification results for 8-class

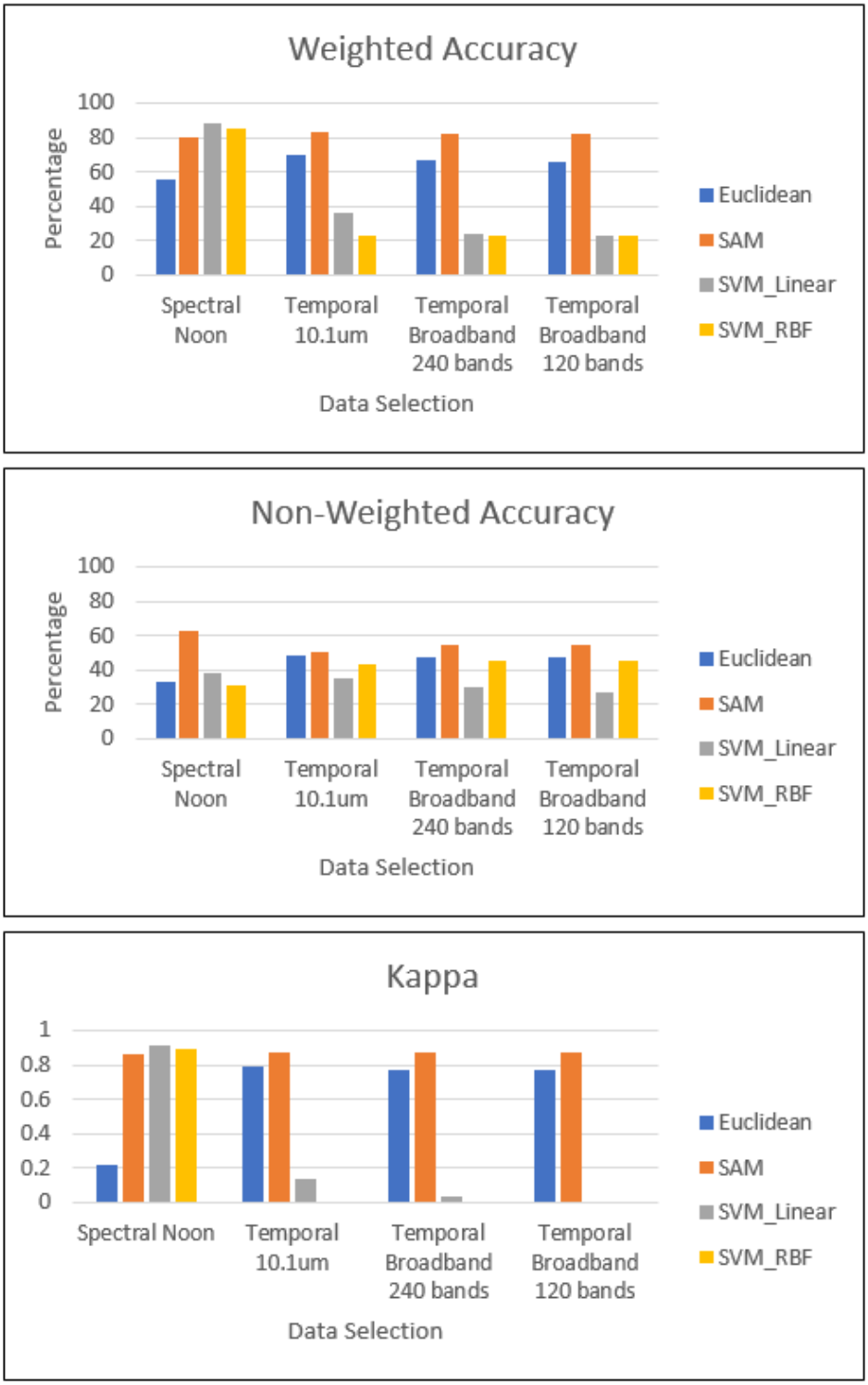

Figure 5.19: Weighted accuracy, non-weighted accuracy and kappa for 8-class classification.

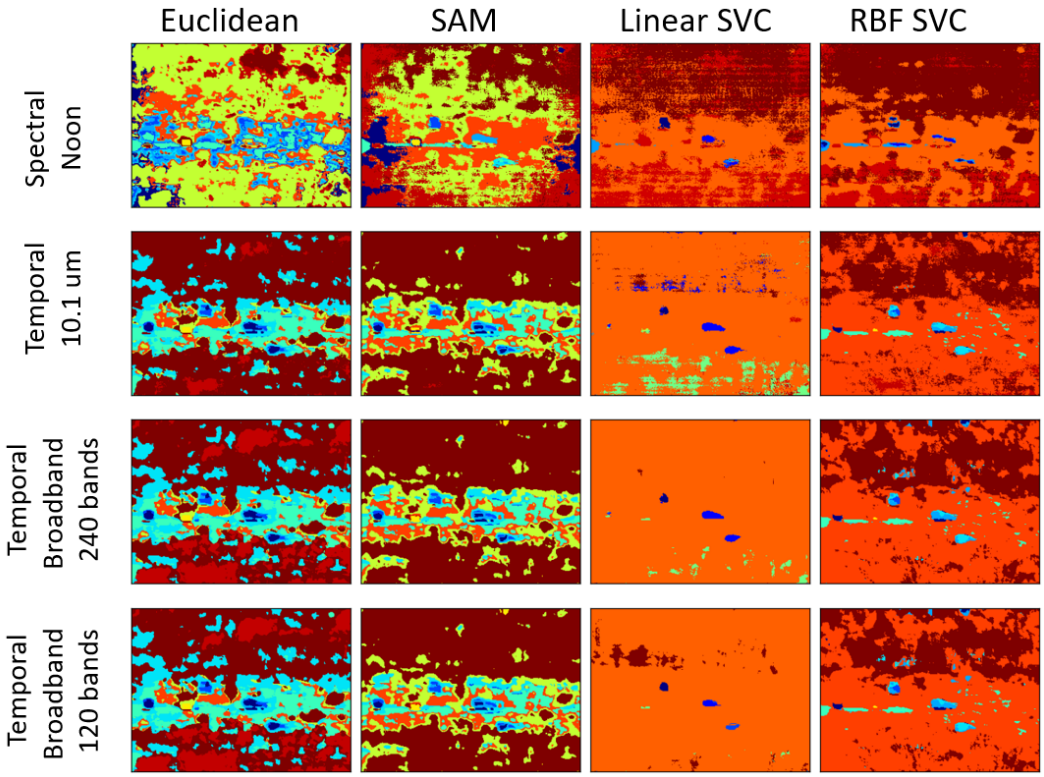

Figure 5.20: Classification results for 10-class

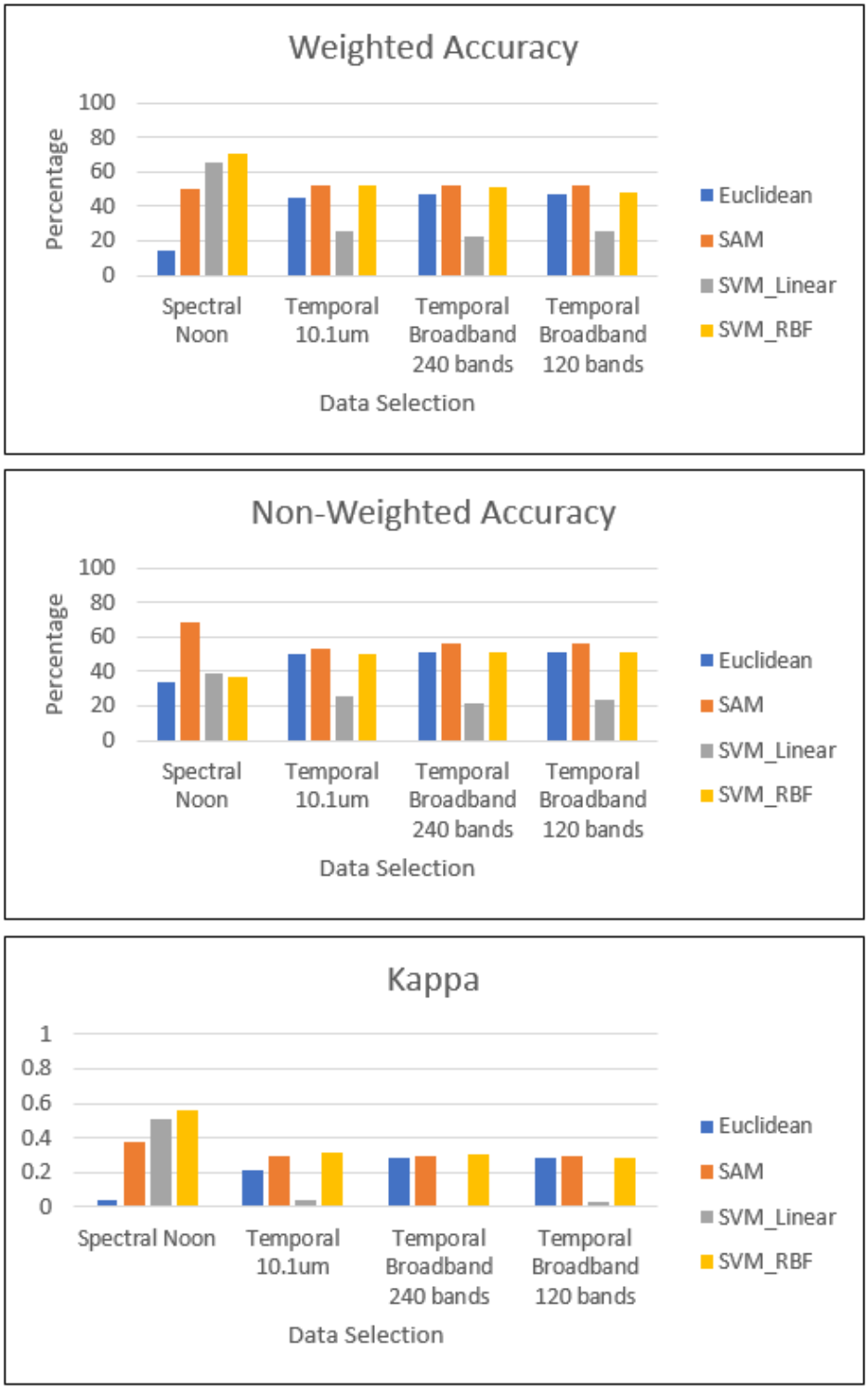

Figure 5.21: Weighted accuracy, non-weighted accuracy and kappa for 10-class classification.

were seen when training and testing data differed. When the temporal cubes were used for supervised classification, the spectral signature results were comparable (or sometimes outperformed) the temporal signature classification as observed in Figures 5.16 to 5.21. This indicated that differences between two diurnal cycles, despite having similar meteorological measurements, will impact classification. The differences between these two diurnal cycles may be caused by slight change in temperature. Some cloud formation earlier on one day (as shown in Figures 5.3 and 5.4) than the other might have delayed the heating of certain materials, causing different temporal signatures. Whereas for the spectral data, the same timeframe data were used for both days, with similar air temperature and relative humidity, which had more probability of having similar spectral signatures.

In terms of physical world application, training and testing cannot be done on the same data. However, this form of analysis is promising despite hypertemporal data underperforming compared to hyperspectral data. For 7-class ground truth class map, hyperspectral data produced a weighted accuracy of 99%, but that does not conclude that using hypertemporal data was a failure. In fact, RBF-240 produced a weighted accuracy of 98.21%. With further analyses, hypertemporal data could be optimized to produce better results when using two different diurnal cycle data.

Chapter 6

Emissivity

Most ARL publications using SPICE dataset used the spectral radiance. The few publications that used emissivity for analysis reported unsuccessful results. This chapter employed four emissivity retrieval algorithms and explored the possibility of using material emissivity for target detection.

6.1 Emissivity Retrieval

Any radiance data collected in the longwave infrared (LWIR) region will be dependent on the object, the atmospheric composition, the time of day and meteorological conditions. While the sensor-reaching radiance will vary for an object, the emissivity of the object should be constant. This unique spectral emissivity per material could be used to identify an object in a scene. The relative emissivity provided in the dataset constantly had values over 1 and could not be taken as accurate emissivities, therefore, attempts were made to estimate the emissivity using the radiance data through few different methods. These included temperature-emissivity separation (TES) using the atmospheric transmission and path radiance based on in-scene atmospheric compensation (ISAC) blackbody normalization [19] [39], alpha-

emissivity method [19][22], QTES [12] [13], and ENvironment for Visualizing Images (ENVI) based emissivity normalization. The various components of the sensor-reaching radiance are illustrated in Figure 6.1. These components are referred in the following sections.

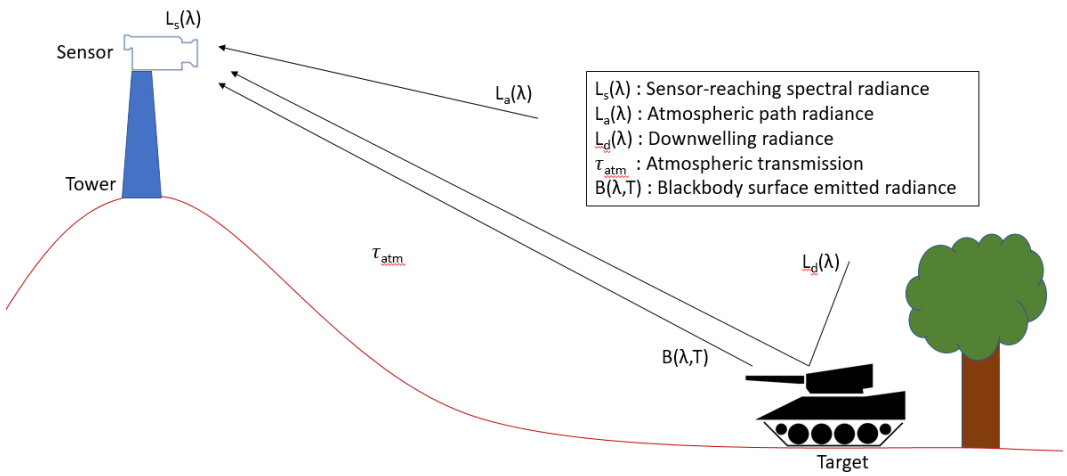

Figure 6.1: Radiative transfer model of the scene describing the various components of the sensor-reaching radiance.

6.1.1 TES using ISAC Blackbody Normalization

For atmospheric compensation, the underlying model is given by:

$$L_s(\lambda) = \tau_{atm}(\lambda)L_u(\lambda) + L_a(\lambda) \tag{6.1}$$

where $L_s(\lambda)$ is the sensor-reaching radiance, $\tau_{atm}(\lambda)$ is the atmospheric transmission, $L_u(\lambda)$ is the upwelling radiance and $L_a(\lambda)$ is the path radiance.

The upwelling radiance model is described by:

$$L_u(\lambda) = \epsilon(\lambda)B(\lambda, T) + [1 - \epsilon(\lambda)]L_d(\lambda) \tag{6.2}$$

where $B(\lambda, T)$ is the blackbody radiance, $\epsilon(\lambda)$ is the material emissivity and $L_d(\lambda)$ is the downwelling radiance.

For a true blackbody, the brightness temperature (Equation 2.1) equals the actual surface temperature. ISAC takes advantage of the natural occurrence of blackbody or near-blackbody objects within the scene. The first step is to approximate $B(\lambda, T)$ from the data, and use it to perform ISAC. The following steps were used for this method.

1. Using the brightness temperature band "image" corresponding to the highest atmospheric transmission (10.102 μm), the radiance ($B(\lambda, T)$) was calculated using the Planck's equation for the applicable wavelengths.

2. Calibrated data cube is represented as $L(\lambda)$. Plot $L(\lambda)$ vs $B(\lambda, T)$, and perform sequential line-fitting as per ref [10]. Six-iterations were conducted for this analysis.

3. The final aggregate slope estimated the atmospheric transmission and the y-intercept estimated the path radiance. Equation 6.1 could be inverted and written as Equation 6.3 using the estimated atmospheric transmission and the path radiance.

$$L_u(\lambda) = \frac{L_s(\lambda) - L_a(\lambda)}{\tau_{atm}(\lambda)} \tag{6.3}$$

However, these are unscaled estimates due to the assumptions that the scene contain true blackbodies and that the brightness temperatures represent true surface temperatures.

4. $\tau_{atm}(\lambda)$ can be scaled through

$$\tau_{atm}(\lambda) = \frac{\tau_o}{\tau_{a,u}(\lambda_o)} \tau_{a,u}(\lambda) \tag{6.4}$$

where $\tau_{a,u}(\lambda)$ is the estimated atmospheric transmission, $\tau_{a,u}(\lambda_o)$ is the atmospheric transmission at the highest transmissive band, and τ_o=0.975 (atmospheric transmission for the highest transmissive band estimated from literature).

5. $L_a(\lambda)$ can be scaled through

$$\begin{aligned} L_a(\lambda) = L_{a,u}(\lambda) + \frac{\tau_{a,u}(\lambda)}{\tau_{a,u}(\lambda_o)} [\alpha(\lambda, \lambda_o)\{\tau_{a,u}(\lambda_o) - \tau_o\} - \\ \beta(\lambda, \lambda_o)\{L_{a,u}(\lambda_o) - (1 - \tau_o)B(\lambda, T_a)\}] \end{aligned} \tag{6.5}$$

where

$$\alpha(\lambda, \lambda_o) = \left(1 - \frac{\lambda}{\lambda_o}\right) B(\lambda, T_o), \tag{6.6}$$

$$\beta(\lambda, \lambda_o) = \frac{\lambda_o}{\lambda} \frac{B(\lambda, T_o)}{B(\lambda_o, T_o)} \tag{6.7}$$

where T_o is the assumed scene temperature (300K for this analysis), T_a is the assumed mean atmospheric temperature (294K for this analysis) and $L_{a,u}(\lambda)$ is the estimated path radiance.

6. The emissivity could be represented by re-arranging Equation 6.2, which results in:

$$\epsilon(\lambda) = \frac{L_u(\lambda) - L_d(\lambda)}{B(\lambda, T) - L_d(\lambda)} \tag{6.8}$$

7. With an assumption that the downwelled radiance is small relative to the emitted radiance due to high emissivity, the downwelled radiance in the numerator and the denominator in Equation 6.8 could be ignored. Thus, emissivity is represented as

$$\epsilon(\lambda) = \frac{L_u(\lambda)}{B(\lambda, T_{max})} \tag{6.9}$$

where T_{max} is the maximum brightness temperature associated with the upwelling radiance.

6.1.2 Alpha Emissivity

The alpha emissivity TES method uses the upwelled radiance calculated in Section 6.1.1, and similar to step 7 from Section 6.1.1, this method

also ignores the downwelled radiance. In addition, it employs the Wien's approximation to the blackbody radiance instead of Planck's law. Planck's law and Wien's approximation are provided in Equations 6.10 and 6.11 respectively.

$$Planck'sLaw = \frac{2hc^2}{\lambda^5 e^{\frac{hc}{\lambda kT}} - 1} \tag{6.10}$$

$$Wien'sApproximation = \frac{2hc^2}{\lambda^5 e^{\frac{hc}{\lambda kT}}} \tag{6.11}$$

Equation 6.9 can be rewritten using Wien's approximation to

$$L_u(\lambda) = \epsilon(\lambda)B(\lambda, T_{max}) \approx \epsilon(\lambda)\frac{2hc^2}{\lambda^5 e^{\frac{hc}{\lambda kT}}} \tag{6.12}$$

By using the subscript n to denote the spectral index of upwelling radiance $L_n = L_u(\lambda_n)$ corresponding to wavelength λ_n, and taking the logarithm and multiplying both sides of Equation 6.12 by the wavelength, Equation 6.12 is written as

$$\lambda_n \ln L_n = \lambda_n \ln \epsilon_n + \lambda_n \ln (2hc^2) - 5\lambda_n \ln \lambda_n - \frac{hc}{kT} \tag{6.13}$$

The spectral average of both sides of Equation 6.13 is

$$\frac{1}{N}\sum_{n=1}^{N}\lambda_n \ln L_n = \frac{1}{N}\sum_{n=1}^{N}\lambda_n \ln \epsilon_n + \ln\left(2hc^2\right)\frac{1}{N}\sum_{n=1}^{N}\lambda_n \\ -5\frac{1}{N}\sum_{n=1}^{N}\lambda_n \ln \lambda_n - \frac{hc}{kT} \tag{6.14}$$

By subtracting Equation 6.13 from Equation 6.14 and re-arranging to have the emissivity term on one side leads to

$$\lambda_n \ln \epsilon_n - \frac{1}{N}\sum_{n=1}^{N}\lambda_n \ln \epsilon_n = \lambda_n \ln \epsilon_n - \frac{1}{N}\sum_{n=1}^{N}\lambda_n \ln L_n + \ln\left(2hc^2\right)\frac{1}{N}\sum_{n=1}^{N}\lambda_n \\ -\lambda_n \ln\left(2hc^2\right) - 5\frac{1}{N}\sum_{n=1}^{N}\lambda_n \ln \lambda_n + 5\lambda_n \ln \lambda_n \tag{6.15}$$

An important characteristic of Equation 6.15 is that it is no longer dependent of the material surface temperature (as opposed to Equation 6.13), as it has been cancelled out. Both sides of Equation 6.15 are defined as alpha emissivity α_n, therefore the alpha emissivity could be computed directly from the upwelling radiance as

$$\alpha_n = \lambda_n \ln \epsilon_n - \frac{1}{N}\sum_{n=1}^{N}\lambda_n \ln L_n + \ln\left(2hc^2\right)\frac{1}{N}\sum_{n=1}^{N}\lambda_n - \lambda_n \ln\left(2hc^2\right) \\ -5\frac{1}{N}\sum_{n=1}^{N}\lambda_n \ln \lambda_n + 5\lambda_n \ln \lambda_n \tag{6.16}$$

Alpha emissivity could then be used to estimate surface emissivity according to

$$\widehat{\epsilon}_n = \epsilon_o e^{\frac{\alpha_n}{\lambda_n}} \tag{6.17}$$

where

$$\epsilon_o = e^{\frac{\overline{\alpha}_n}{\lambda_n}} \tag{6.18}$$

and

$$\overline{\alpha}_n = \frac{1}{N} \sum_{n=1}^{N} \lambda_n \ln \epsilon_n \tag{6.19}$$

In order to estimate the scaling factor ϵ_o, the emissivity calculated in Equation 6.9 was used in Equation 6.19.

6.1.3 Quick Temperature Emissivity Separation

The distance from the sensor to the targets was small, and estimating the atmospheric parameters using conventional methods for such distance was difficult. In order to solve and mitigate this issue, Christoph Borel came up with QTES. This section describes the QTES method in detail [11]. Referring to the model described in Equation 6.1 with Equation 6.2 included yield to Equation 6.20. The sensor-reaching radiance is described in equation 6.20 where L(λ) is the sensor-reaching radiance, ϵ is the material emissivity, τ_{atm} is the atmospheric transmission, B(T,λ) is the blackbody radiance of the material, $L_d(\lambda)$ is the downwelling radiance and $L_a(\lambda)$ is the path radiance.

$$L(\lambda) = \epsilon B(T, \lambda)\tau_{atm} + (1 - \epsilon)L_d(\lambda) + L_a(\lambda) \tag{6.20}$$

QTES uses the in-scene aluminum panel assuming it is a perfect reflector. For a perfect reflector, the emissivity will be zero and thus equation 6.20 could be approximated to:

$$L(\lambda) \approx L_d(\lambda) + L_a(\lambda) \tag{6.21}$$

Therefore, the sky plate radiance is the sum of the downwelling and path radiances. The atmospheric transmission, path randiance and downwelling radiance are calculated using MODTRAN models.

For each pixel:

1. The brightness temperature is calculated using Equation 2.1 for a high transmission band, in this case the band corresponding to 10.102 μm (the calculated brightness temperature is verified with the provided brightness temperature).

2. A range of emissivity is calculated by re-arranging Equation 6.20 as per Equation 6.22.

$$\epsilon_k = \frac{L_s - L_d - L_a}{B(T_k, \lambda)\tau_{atm} - L_d} \tag{6.22}$$

   where L_s is the sensor-reaching radiance and T_k is a range of temperatures calculated using Equation 6.23.

$$T_k = \{T_{BB} - \frac{K}{2dT} + kdT\}, k = 1, 2, ..., K \tag{6.23}$$

where T_{BB} is the brightness temperature calculated earlier, dT is increment of 1, and K is the range of selected temperatures. In this case, K=20 was used to calculated 20 different temperatures.

3. For a narrow spectral range (9.5-10 μm), the optimal temperature (T_{opt}) is retrieved. T_{opt} is found by finding the variance in emissivity within the spectral range, and locating the emissivity with the smallest variance between the 20 emissivity variances. Using the smallest variance, the corresponding temperature is declared to be T_{opt}.

Emissivity is calculated using Equation 6.22 where T_{opt} replaces T_k, and the MODTRAN model atmospheric transmission, path radiance and downwelling radiance are τ_{atm}, L_u and L_d respectively, and L_s is the radiance data from the calibrated radiance cube. This was the method used to retrieve the provided relative emissivity cubes.

6.1.4 ENVI Based Emissivity Normalization

The built-in ENVI [2] algorithms were used to retrieve emissivity. Prior to retrieving emissivity, the data needed to be compensated for atmospheric effects. This is performed using the built-in Thermal Atmospheric Correction algorithm. The Thermal Atmospheric Correction approximates and removes

the atmospheric contributions from thermal infrared radiance data. This algorithm assumes that the atmosphere is uniform over the data scene and a near-blackbody object is present in the scene. It also ignores the reflected downwelled radiance.

Once the radiance data is obtained following atmospheric compensation, Emissivity Normalization algorithm is applied. This algorithm uses the highest temperature for each pixel to calculate the emissivity values using the Planck equation.

6.2 Emissivity Retrieval Results

For each of the emissivity retrieval algorithms described in Section 6.1, two plots will be displayed. The first plot will showcase the emissivity of two manmade materials (Tank0 and black panel) and two natural materials (grass and gravel) for a given time of day. This plot will enable to differentiate the spectral differences between each material. The second plot will showcase the emissivity of Tank0 for a full diurnal cycle (all the data cubes in a 24-hrs period). The second plot should provide a "single" emissivity spectrum irrespective of the time of day since the emissivity is an instrinsic characteristic of the material that does not change with time.

6.2.1 TES using ISAC Blackbody Normalization

While calculating emissivity using the alpha emissivity separation methods, some values ended up being negative values. Since negative emissivity was

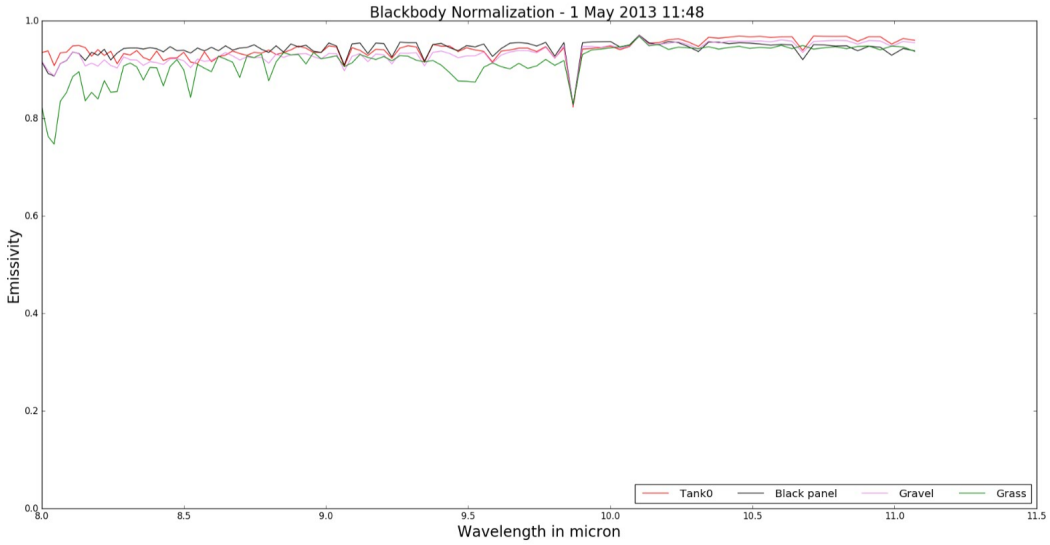

Figure 6.2: Emissivity of four distinct materials calculated using the blackbody normalization technique for data corresponding to 11:48, 1 May 2013.

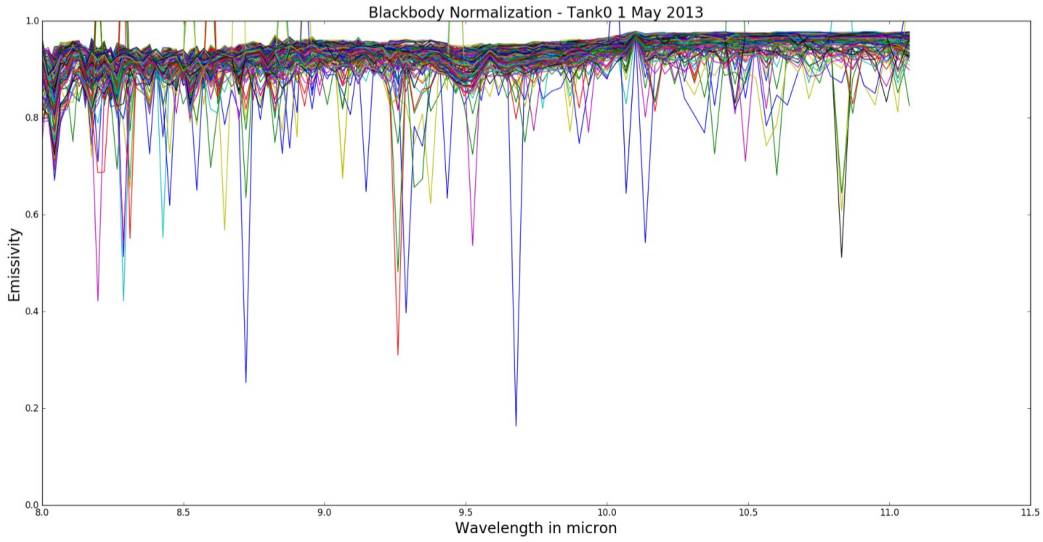

Figure 6.3: Emissivity of Tank0 calculated using the blackbody normalization technique for data from 1 May 2013 (diurnal cycle). NOTE: Emissivities containing negative values following calculation have been omitted in this plot.

not physically possible (most likely the result of various assumptions made for this method), the emissivity spectra containing negative values were omitted when plotting Figure 6.3.

Figure 6.2 shows that there are some spectral differences between the materials (notably grass and Tank0). However, when the tank emissivity spectra were plotted for a 24-hr period (Figure 6.3), it was clear that the retrieved emissivity from blackbody normalization was not accurate.

6.2.2 Alpha Emissivity

There were no clear and consistent spectral differences between the material emissivities as observed in Figure 6.4. We could conclude that the emissivity retrieved was not viable for any further analysis.

Figure 6.5 used 252 emissivity cubes from 12 Aug 2012 diurnal cycle. It was very noticeable that there was a big range in emissivity spectrum of the same material, supporting our earlier conclusion that the emissivity estimates were not accurate.

6.2.3 Quick Temperature Emissivity Separation

The relative emissivity data provided by ARL were calculated via QTES algorithm. Since it contained emissivity values greater than 1 (which cannot be physically explained), we could not take the given data as is and we attempted to run the QTES algorithm from scratch. Our results also resembled the results obtained by ARL, where emissivity values greater than 1 were frequently

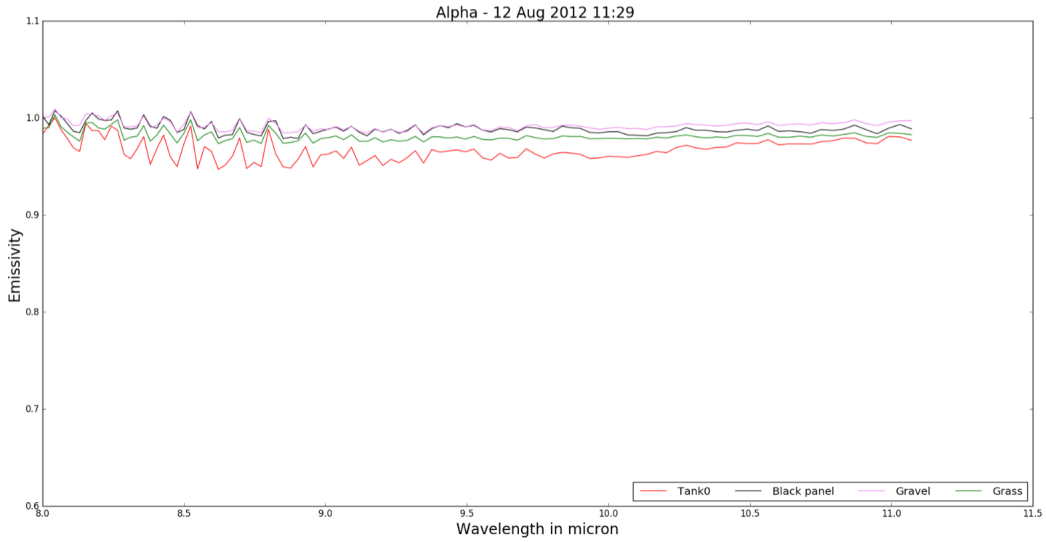

Figure 6.4: Emissivity of four distinct materials calculated using the alpha emissivity separation technique for data corresponding to 11:29, 12 Aug 2012.

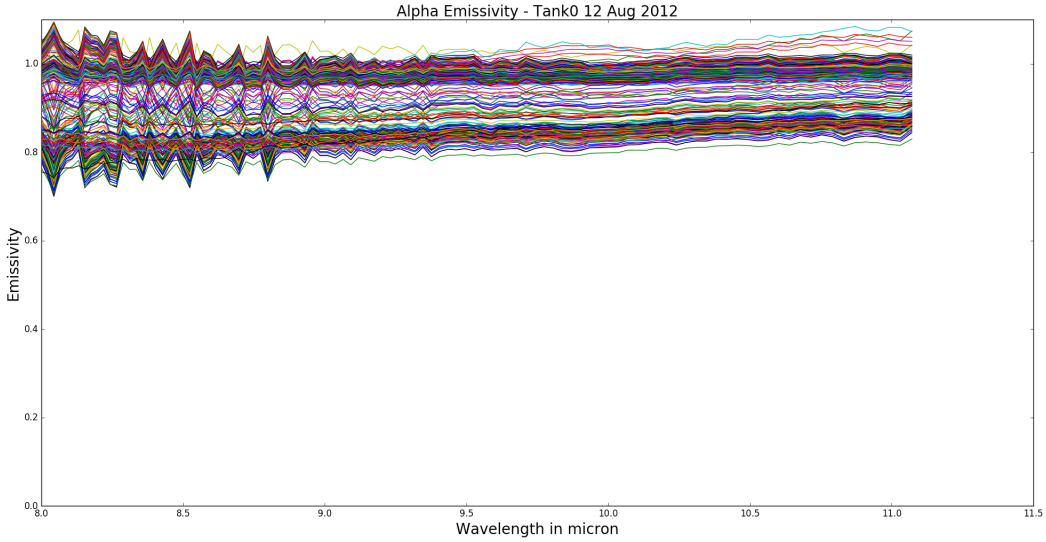

Figure 6.5: Emissivity of Tank0 calculated using the alpha emissivity separation technique for data from 12 Aug 2012.

observed as seen on Figure 6.6. In addition, the tank emissivity spectra were not close to each other for different timeframes as seen on Figure 6.7.

6.2.4 ENVI Based Emissivity Normalization

Our last method to retrieve emissivity was fully based on ENVI. Yet, even in this method, there was no spectral uniqueness in materials as observed in Figure 6.8. In addition, there was a large range in the Tank0's emissivity spectrum for different timeframes as displayed in Figure 6.9. The emissivity obtained using ENVI also cannot be used for further analysis.

Despite using four methods to retrieve emissivity (three algorithms implemented in Python and one based on built-in ENVI functions), physically-plausible emissivity data were not obtained in order to be able to conduct any analysis. First, there was not adequate spectral uniqueness between the materials, even the expected Reststrahlen feature in gravel was not observed. Furthermore, when the emissivity of one material from different timeframes was plotted, the range between them was far too great to consider the result was in fact the true material emissivity. No further analysis could be done using the emissivity obtained so far using these methods.

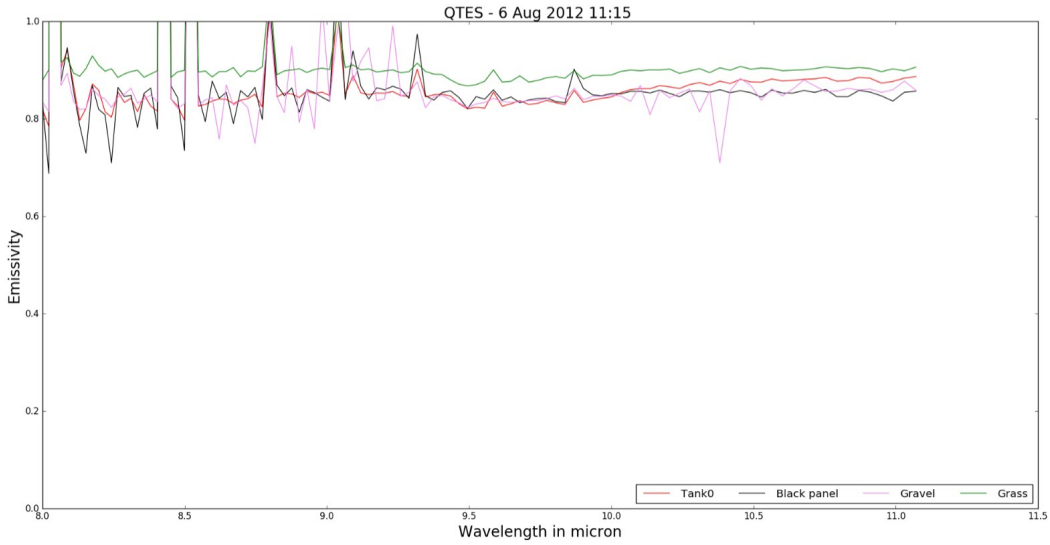

Figure 6.6: Emissivity of four distinct materials calculated using the QTES technique for data corresponding to 11:15, 6 Aug 2012.

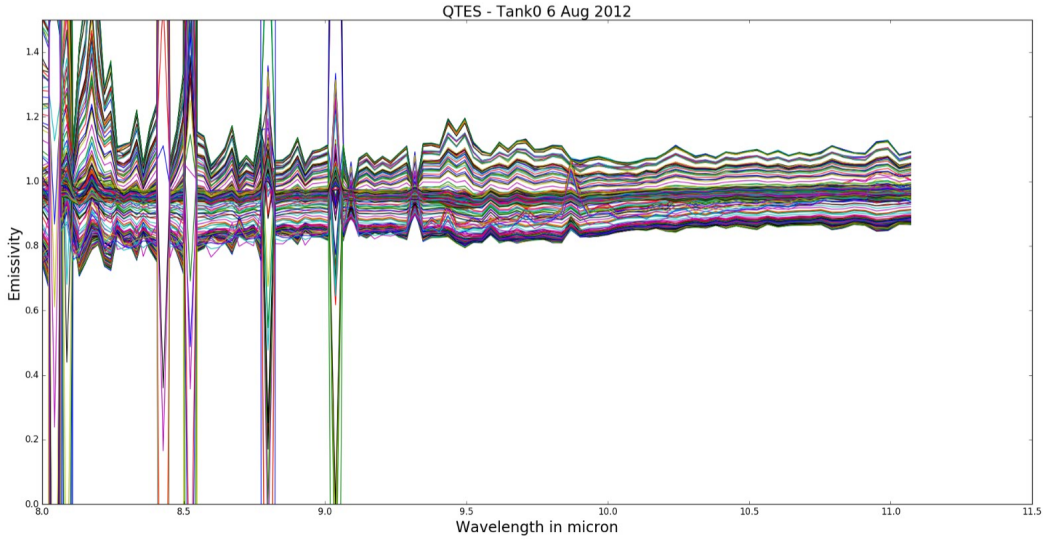

Figure 6.7: Emissivity of Tank0 calculated using the QTES technique for all data from 6 Aug 2012 (diurnal cycle).

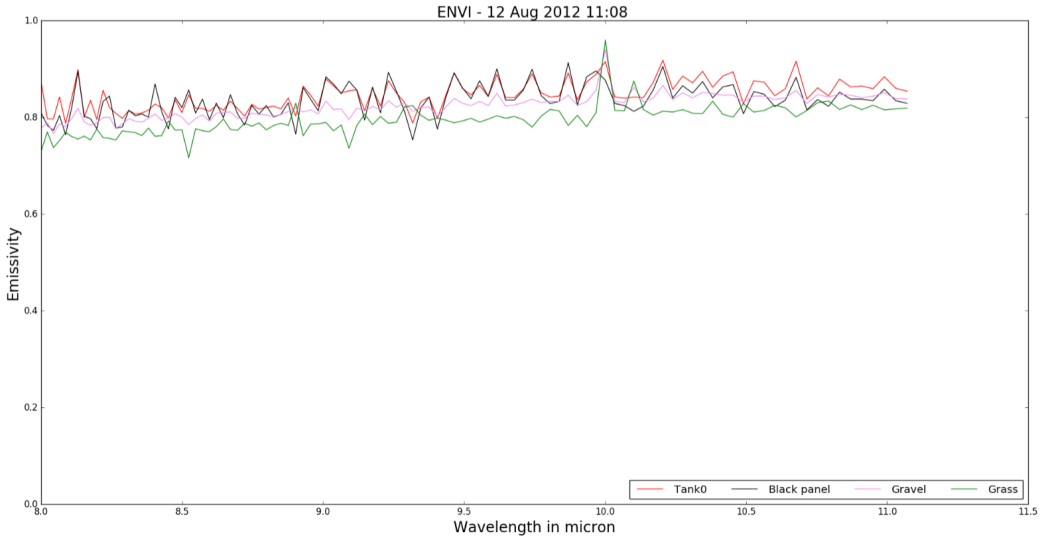

Figure 6.8: Emissivity of four distinct materials calculated using ENVI for data corresponding to 11:08, 12 Aug 2012.

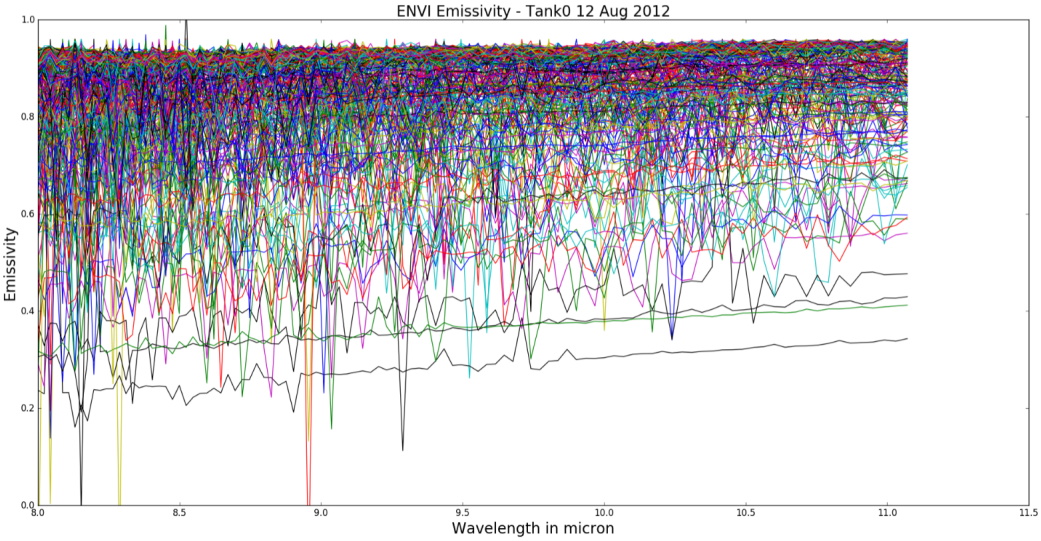

Figure 6.9: Emissivity of Tank0 calculated using ENVI for data from 12 Aug 2012.

Chapter 7

Summary and Future Work

This section summarizes what has been done on the hyperspectral and hypertemporal LWIR dataset provided to RIT by ARL. The SPICE data collection was described in detail, including the location of the collection, the sensor used, the contents of the scene, and the calibrated data provided by ARL.

The impacts of precipitation on the collection of the data were visualized using five different meteorological conditions from the same diurnal cycle. It was found that hail and rain adversely affected the quality of the collected data, and no further analyses were performed on the data collected during precipitation events.

The first task carried out using this dataset was to confirm the SPICE data with MODTRAN simulation. The simulation resulted in similar values to the SPICE dataset which indicated that the data were dependable and realistic, and further analysis could be carried out. Yet, it was decided to check the quality of the dataset prior to embarking on the next goal. While performing quality check, it was discovered there were many unusable data cubes in the dataset, in that the values in these cubes were not realistic and

broke pattern with the adjacent cubes. These cubes were found to be taken right after the hourly blackbody measurements. These 339 erroneous data cubes were removed from analysis conducted in this thesis.

The instrument noise was characterized using the black panel from the scene. The calculated instrument noise was comparable to the manufacturer's specified NESR. The noise was also visually represented using the noise correlation coefficient matrix.

The mean variation for a full diurnal cycle was displayed for eight materials from the scene. The standard deviation variation for a full diurnal cycle was also displayed for the same eight materials.

Spatial variation was shown for black panel, white panel, tanks and grass for noon and midnight timeframes.

Tank target detection was also conducted using this dataset. Using the target spectrum at one time, three target detection algorithms including ACE, SAM and SMF were applied to find the targets at different times for a full diurnal cycle. It was found that SMF works best for detecting the targets for both noon and midnight target spectra. Hyperspectral and hypertemporal unsupervised and supervised classification were conducted extracting features from 1 May 2013 and testing on 2 May 2013 data. Using weighted accuracy, non-weighted accuracy and kappa as comparison metrics, it was discovered that the hyperspectral cubes performed overall better than the hypertemporal cubes.

The last task to be carried out was the retrieval of emissivity estimates with the goal of using this metric for target detection and material identification. Four temperature-emissivity separation methods (temperature-emissivity separation using the atmospheric transmission and path radiance based on in-scene atmospheric compensation blackbody normalization, alpha-emissivity method, Quick Temperature-Emissivity Separation, and ENVI based emissivity normalization) were used to estimate material emissivity. The results from all four methods were not acceptable for data analysis for two main reasons. One, there was not much spectral differences between two materials in the estimated emissivities. This will not yield adequate result in either target detection or material identification. Two, the range in spectral emissivity for one material were too large between different timeframes. We expected differences due to different factors from one time to another, but the range observed in the produced result was not explainable, other than that they do not represent well the material emissivity.

For future work, a recommendation is to analyze further the results observed in Figure 4.20, where the grass shared a similar trend to gravel than other vegetation types. Research could be conducted using linear mixing model to test the abundance of materials in each pixel and quantify the reason for this unexpected observation.

Another recommendation is to perform noise-reduction techniques on the calibrated radiance data and use them for the emissivity retrieval algorithms as performed in this thesis. This may improve the results for emissivity

estimation and the results may be used for material identification.

It would be interesting to perform image classification using different models of hypertemporal data than examined in this thesis. It was noted that hypertemporal data's weighted accuracy was close to the hyperspectral data's weighted accuracy for 7-class ground truth class map. Building different hypertemporal data models may surpass the models studied in this thesis.

Appendices

Appendix A

Inconsistent Data

Table A.1: Inconsistent SPICE dataset files

Date	Number of hdf5 files containing inconsistent data *(filenumber)*
2012_07_27	5 *(33,44,88,99,110)*
2012_07_30	8 *(11,22,33,66,77,88,132,143)*
2012_07_31	10 *(44,55,66,109,120,131,142,175,186,197)*
2012_08_01	11 *(44,55,99,110,121,165,176,187,231,242,253)*
2012_08_02	13 *(22,33,44,88,99,110,154,165,176,187,231,242,253)*
2012_08_03	12 *(33,44,55,99,110,121,132,176,187,198,209,253)*
2012_08_04	13 *(11,22,77,88,99,110,154,165,176,187,231,242,253)*
2012_08_05	12 *(22,33,44,88,99,110,154,165,176,187,242,253)*
2012_08_06	11 *(44,55,66,99,110,121,165,176,187,198,253)*
2012_08_07	8 *(11,55,66,77,121,132,143,154)*
2012_08_10	8 *(11,22,66,77,88,132,143,154)*
2012_08_11	14 *(22,33,44,55,88,99,110,121,154,165,176,220,232,242)*
2012_08_12	12 *(22,33,44,77,88,99,143,154,165,209,220,231)*
2012_08_13	14 *(11,22,33,44,77,88,99,143,154,165,176,220,231,242)*
2012_08_14	12 *(22,33,44,88,99,110,143,154,165,209,220,231)*
2012_09_04	4 *(8,19,30,41)*
2012_09_05	12 *(11,22,33,88,97,108,119,130,185,196,207,218)*
2012_09_06	13 *(11,22,33,77,88,99,143,154,165,176,231,242,253)*
2013_05_01	23 *(10,21,32,43,54,65,76,87,98,109,120,131,142,153,164,175,186, 197,208,219,230,241,252)*
2013_05_02	23 *(10,21,32,43,54,65,76,87,98,109,120,131,142,153,164,175,186, 197,208,219,230,241,252)*
2013_05_03	23 *(10,21,32,43,54,65,76,87,98,109,120,131,142,153,164,175,186, 197,208,219,230,241,252)*
2013_05_04	21 *(10,21,32,54,65,76,87,98,109,120,131,142,153,164,175,186, 208,219,230,241,252)*
2013_05_05	22 *(10,21,32,43,54,65,76,87,98,109,120,131,142,164,175,186, 197,208,219,230,241,252)*
2013_05_06	13 *(10,21,32,43,54,65,76,87,98,109,120,131)*
2013_05_07	14 *(7,18,29,40,51,62,73,84,95,117,128,139,150,161)*
2013_05_08	8 *(10,21,32,42,52,63,74,85)*

Appendix B

MODTRAN Input Cards

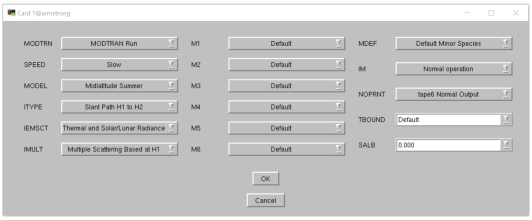

Figure B.1: Card 1

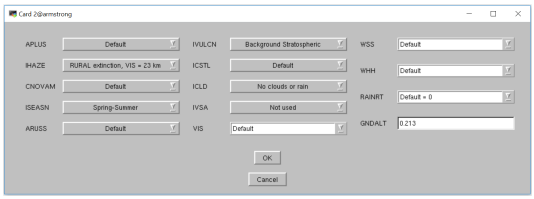

Figure B.2: Card 2

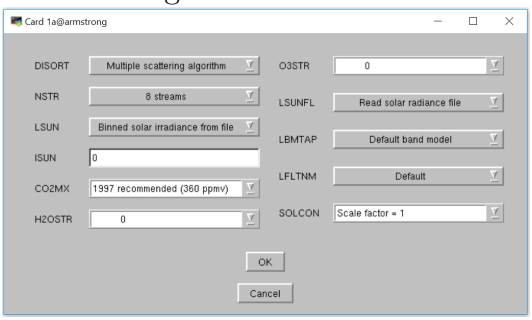

Figure B.3: Card 1A

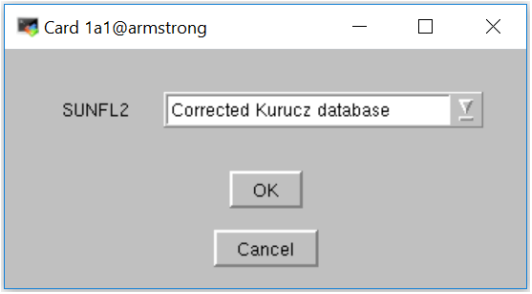

Figure B.4: Card 1A1

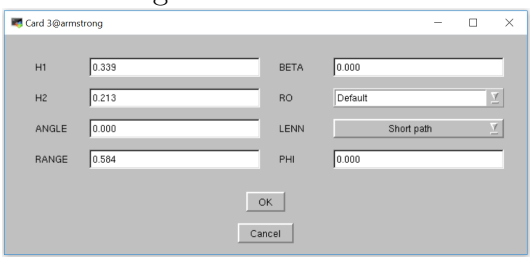

Figure B.5: Card 3

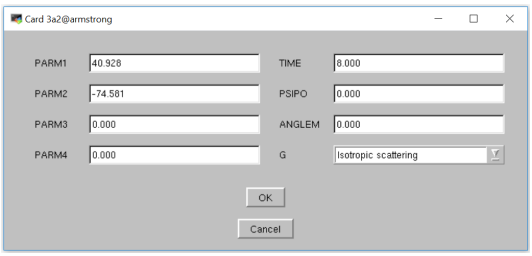

Figure B.6: Card 3A2

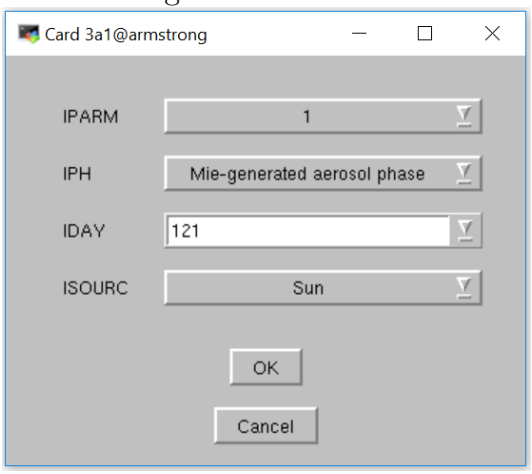

Figure B.7: Card 3A1

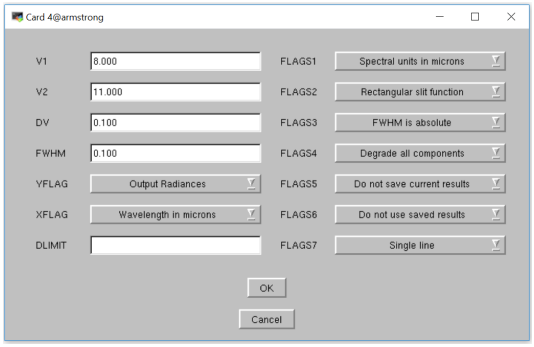

Figure B.8: Card 4

Bibliography

[1] Emissivity definition. http://www.npl.co.uk/reference/faqs/what-is-/emissivity-and-why-is-it-important-(faq-thermal). Accessed: 2017-05-26.

[2] Envi algorithms. https://www.harrisgeospatial.com/docs/Atmospheric/Correction.html. Accessed: 2016-12-10.

[3] Google maps - targets and tower. https://www.google.com/maps/place/40%C2%B055'49.5%22N+74%C2%B035'13.4%22W/@40.930834,-74.6013787,5250m/data=!3m1!1e3!4m5!3m4!1s0x0:0x0!8m2!3d40.930414!4d-74.587059. Accessed: 2017-01-16.

[4] Hypertemporal imaging space experiment. http://www.spectral.com/Success_HTISpX.shtml. Accessed: 2017-05-10.

[5] Modtran. http://modtran.spectral.com/. Accessed: 2017-05-30.

[6] Satellite hsi dataset with ground-truth. http://www.ehu.eus/ccwintco/index.php?title=Hyperspectral_Remote_Sensing_Scenes. Accessed: 2017-03-23.

[7] Spectir free data samples. http://www.spectir.com/free-data-samples/. Accessed: 2017-03-23.

[8] Svm: Linear and rbf svc. `http://contrib.scikit-learn.org/py-earth/auto_examples/plot_classifier_comp.html`. Accessed: 2017-05-03.

[9] Who invented camera. `http://www.whoinvented.org/who-invented-camera/`. Accessed: 2017-03-22.

[10] C. Borel. Error analysis for a temperature and emissivity retrieval algorithm for hyperspectral imaging data. *International Journal of Remote Sensing*, 29:5029–5045, 2008.

[11] C. Borel, D. Rosario, and J. Romano. Range-invariant anomaly detection applied to imaging fourier transform spectrometry data. In S.S. Shen and P.E. Lewis, editors, *Imaging Spectrometry XVII*, volume 8515 of *Proc. SPIE*, 2012.

[12] C. Borel, D. Rosario, and J. Romano. Analysis of diurnal, long-wave hyperspectral measurements of natural backgorund and manmade targets under different weather conditions. In *Applied Imagery Pattern Recognition Workshop (AIPR), 2014 IEEE*, volume 1, 2014.

[13] C. Borel, D. Rosario, and J. Romano. Data processing and temperature-emissivity separation for tower-based imaging Fourier transform spectrometer data. *International Journal of Remote Sensing*, 36(19-20):4779–4792, 2015.

[14] M. Borengasser, W.S. Hungate, and R. Watkins. *Hyperspectral Remote Sensing : Principles and Applications*. CRC Press, Boca Raton, Florida,

first edition, 2008.

[15] M. Chilton, S.J. Walsh, and D.S. Daly. Prediction metrics for chemical detection in long-wave infrared hyperspectral imagery. *Journal of Undergraduate Research*, 9:48–52, 2015.

[16] P. Coppin, I. Jonckheere, K. Nackaerts, and B. Muys. Digital change detection methods in ecosystem monitoring: a review. *International Journal of Remote Sensing*, 25(9):1565–1596, 2004.

[17] C.A. de Bie, M.R. Khan, A.G. Toxopeus, V. Venus, and A.K. Skidmore. Hypertemporal image analysis for crop mapping and change detection. In *International Society for Phtogrammetry and Remote Sensing*, volume VII of *Proc. of the XXI congress:*, pages 808–812, 2008.

[18] A. Dergevorkian and K. McKee. Hyperspectral/hypertemporal compact sensor for small satellite applications. In *Conference on Small Satellites*, volume 24th Annual AIAA/USU of *Proc. of the XXI congress:*, 2010.

[19] M.T. Eismann. *Hyperspectral Remote Sensing*. SPIE Press, Bellingham, Washington, first edition, 2012.

[20] H. Huang and C. Lin. Linear and kernel classification: When to use which? In *Proceedings of the 2016 SIAM International Conference on Data Mining*, pages 216–224, 2016.

[21] J.E. Johnson, J.A. Shaw, R. Lawrence, P.W. Nugent, L.M. Dobeck, and L.H. Spangler. Long-wave infrared imaging of vegetation for detecting leaking co2 gas. *Journal of Applied Remote Sensing*, 6:06361–1, 2012.

[22] P.S. Kealy and S.J. Hook. Separating Temperature and Emissivity in Thermal Infrared Multispectral Scanner Data: Implications for Recovering Land Surface Temperatures. *Transactions on Geoscience and Remote Sensing*, 31(6):1155–1164, 1993.

[23] A. Lausch, M. Pause, A. Schmidt, C. Salbach, S. Gwillym-Margianto, and I. Merbach. Temporal hyperspectral monitoring of chlorophyll, lai, and water content of barley during a growing season. *Canadian Journal of Remote Sensing*, 39:191–207, 2013.

[24] T. Marrinan, J.R. Beveridge, B. Draper, M. Kirby, and C. Peterson. Flag-based detection of weak gas signatures in long-wave infrared hyperspectral image sequences. In Miguel Velez-Reyes and David W. Messinger, editors, *Algorithms and Technologies for Multispectral, Hyperspectral, and Ultraspectral Imagery XXII*, volume 9840 of *Proc. SPIE*, 2016.

[25] D.W. Messinger, C. Salvaggio, and N.M. Sinisgalli. Detection of gaseous effluents from airborne lwir hyperspectral imagery using physics-based signatures. *International Journal of High Speed Electronics and Systems*, 2011.

[26] P. Rauss and D. Rosario. Deep greedy learning under thermal variability in full diurnal cycles. *Optical Engineering*, 2017.

[27] R.Marwha, A.Kumar, and A.S. Kumar. Object-oriented and pixel-based classification approach for land cover using airborne long-wave infrared hyperspectral data. *Journal of Applied Remote Sensing*, 9:095040–1, 2015.

[28] J. Romano, D. Rosario, V. Farley, D. Chenault, and B. Sohr. Spectral and Polarimetric Imagery Collection Experiment. *Army Research Lab Technical Report ARMET-TR-11027*, 2011.

[29] J. Romano, D. Rosario, V. Farley, and B. Sohr. Spectral imagery collection experiment. In S.S. Shen and P.E. Lewis, editors, *Algorithms and Technologies for Multispectral, Hyperspectral, and Ultraspectral Imagery XVI*, volume 7695 of *Proc. SPIE*, 2010.

[30] D. Rosario. Personal communication, February 8, 2017.

[31] D. Rosario, C. Borel, and J. Romano. Against conventional wisdom: Longitudinal inference for pattern recognition in remote sensing. In *Applied Imagery Pattern Recognition Workshop (AIPR), 2014 IEEE*, pages 1–10, 2014.

[32] D. Rosario, C. Borel, and J. Romano. Solid target spectral variability in lwir. In M. Velez-Reyes and D.W. Messinger, editors, *Algorithms and Technologies for Multispectral, Hyperspectral, and Ultraspectral Imagery XXII*, volume 9840 of *Proc. SPIE*, 2016.

[33] D. Rosario and J. Romano. Typical data models are inadequate for hypertemporal imagery. In *IGARSS*, 2015.

[34] D. Rosario, J. Romano, and C. Borel. First observations using spice hyperspectral dataset. In M. Velez-Reyes and F.A. Kruse, editors, *Algorithms and Technologies for Multispectral, Hyperspectral, and Ultraspectral Imagery XX*, volume 9088 of *Proc. SPIE*, 2014.

[35] D. Rosario, J. Romano, and C. Borel. Spectral and Polarimetric Imagery Collection Experiment (SPICE) Longwave Infrared Spectral Dataset. *Army Research Lab Technical Report 7051*, 2014.

[36] D. Rosario, J. Romano, and C. Borel. Pattern recognition in hyperspectral persistent imaging. In M. Velez-Reyes and F.A. Kruse, editors, *Algorithms and Technologies for Multispectral, Hyperspectral, and Ultraspectral Imagery XXI*, volume 9472 of *Proc. SPIE*, 2015.

[37] J.R. Schott. *Remote Sensing: The Image Chain Approach*. Oxford University Press, 198 Madison Avenue, NY, second edition, 2007.

[38] T. Skauli and J. Farrell. A collection of hyperspectral images for imaging systems research. In *Digital Photography IX*, volume 8660 of *Proc. SPIE*, 2013.

[39] S.J. Young, B.R Johnson, and J.A. Hackwell. An in-scene method for atmospheric compensation of thermal hyperspectral data. *Journal of Geophysical Research*, 107(D24):4774, 2002.

[40] W.W. Zhang and S. Sriharan. Using hyperspectral remote sensing for land cover classification. In *Multispectral and Hyperspectral Remote Sensing Instruments and Applications II*, volume 5655 of *Proc. SPIE*, 2005.